Transient Response of the Southern Ocean to Idealized Wind and Thermal Forcing across Different Model Resolutions

QIAN LI,[a] MATTHEW H. ENGLAND,[b] AND ANDREW MCC. HOGG[c]

[a] *Climate Change Research Centre and ARC Centre of Excellence for Climate System Science, University of New South Wales, Sydney, New South Wales, Australia*

[b] *Climate Change Research Centre and ARC Centre of Excellence for Climate Extremes, University of New South Wales, Sydney, New South Wales, Australia*

[c] *Research School of Earth Sciences and ARC Centre of Excellence for Climate Extremes, Australian National University, Canberra, Australian Capital Territory, Australia*

(Manuscript received 18 December 2020, in final form 19 March 2021)

ABSTRACT: The Southern Ocean has undergone significant climate-related changes over recent decades, including intensified westerly winds and increased radiative heating. The interplay between wind-driven cooling and radiative warming of the ocean is complex and remains unresolved. In this study, idealized wind and thermal perturbations are analyzed in a global ocean–sea ice model at two horizontal resolutions: nominally, 1° and 0.1°. The sea surface temperature (SST) response shows a clear transition from a wind-driven cooling phase to a warming phase. This warming transition is largely attributed to meridional and vertical Ekman heat advection, which are both sensitive to model resolution due to the model-dependent components of temperature gradients. At higher model resolution, due to a more accurate representation of near-surface vertical temperature inversion and upward Ekman heat advection around Antarctica, the anomalous SST warming is stronger and develops earlier. The mixed layer depth at midlatitudes initially increases due to a wind-driven increase in Ekman transport of cold dense surface water northward, but then decreases when the thermal forcing drives enhanced surface stratification; both responses are more sensitive at lower model resolution. With the wind intensification, the residual overturning circulation increases less in the 0.1° case because of the adequately resolved eddy compensation. Ocean heat subduction penetrates along more tilted isopycnals in the 1° case, but it orients to follow isopycnal layers in the 0.1° case. These findings have implications for understanding the ocean response to the combined effects of Southern Hemisphere westerly wind changes and anthropogenic warming.

KEYWORDS: Southern Ocean; Ocean dynamics; Ocean models; Climate change; Annular mode

1. Introduction

The Southern Ocean has played a vital role in moderating the increased radiative trapping of heat by greenhouse gases in recent decades, via transporting and sequestering vast quantities of anthropogenic heat (Roemmich et al. 2015; Frölicher et al. 2015) and carbon (Khatiwala et al. 2009; Frölicher et al. 2015; Gruber et al. 2019). Transport of heat and carbon across the base of the mixed layer, closely tied to the formation of Subantarctic Mode Water (SAMW; McCartney 1977; Rintoul and England 2002), is one of the key pathways to sequestration (Sarmiento et al. 2004; Sallée et al. 2012). Most pervasive areas of deep mixed layers form in the Southern Ocean, particularly on the equatorward flank of the Antarctic Circumpolar Current (ACC; McCartney 1977; Dong et al. 2008). The deepening of winter mixed layers gives rise to the subduction of surface waters to the thermocline and intermediate layers, where mode and intermediate waters are formed and carry their physical properties equatorward via the subtropical gyre interior flows (England et al. 1993; Sloyan and Rintoul 2001; Downes et al. 2011). This ventilation of the permanent pycnocline along the path of the upper limb of the Southern Ocean overturning circulation (Sloyan and Rintoul 2001; Lumpkin and Speer 2007) provides a mechanism for long-term climate memory (Fraedrich et al. 2004; Primeau and Holzer 2006).

A key driver of the Southern Ocean circulation is the prevailing westerly winds, which are the strongest mean surface winds on Earth. The Southern Hemisphere westerlies principally force the deep-reaching and eastward-flowing ACC around the globe (Nowlin and Klinck 1986; Orsi et al. 1995). The westerly winds also control northward Ekman transport (Rintoul and England 2002) and the resultant Ekman upwelling around the Antarctic continent (Morrison et al. 2015; Hogg et al. 2017). The resulting upwelling of nutrient-rich deep waters closes a global-scale return pathway for the dense water in sinking regions to ultimately return to the surface (Marshall and Speer 2012; Morrison et al. 2015). Global satellite data records of significant wave height have been used to infer that the Southern Hemisphere westerlies have experienced increases of approximately $+20\,\mathrm{cm\,s^{-1}}$ per decade from 1985 to 2018 (Young and Ribal 2019). An intensification and poleward shift of the westerly winds correspond to a trend toward the positive phase of the southern annular mode (SAM; Gong and Wang 1999; Limpasuvan and Hartmann 1999; Thompson and Wallace 2000; Thompson et al. 2011; Jones et al. 2016) primarily caused by stratospheric ozone depletion (Gillett and Thompson 2003; Marshall et al. 2004; Polvani et al. 2011). Previous studies suggest that the recent wind intensification has likely contributed to a faster rate of ocean heat uptake (Cai et al. 2010) and ocean

Corresponding author: Qian Li, qian.li5@unsw.edu.au

DOI: 10.1175/JCLI-D-20-0981.1

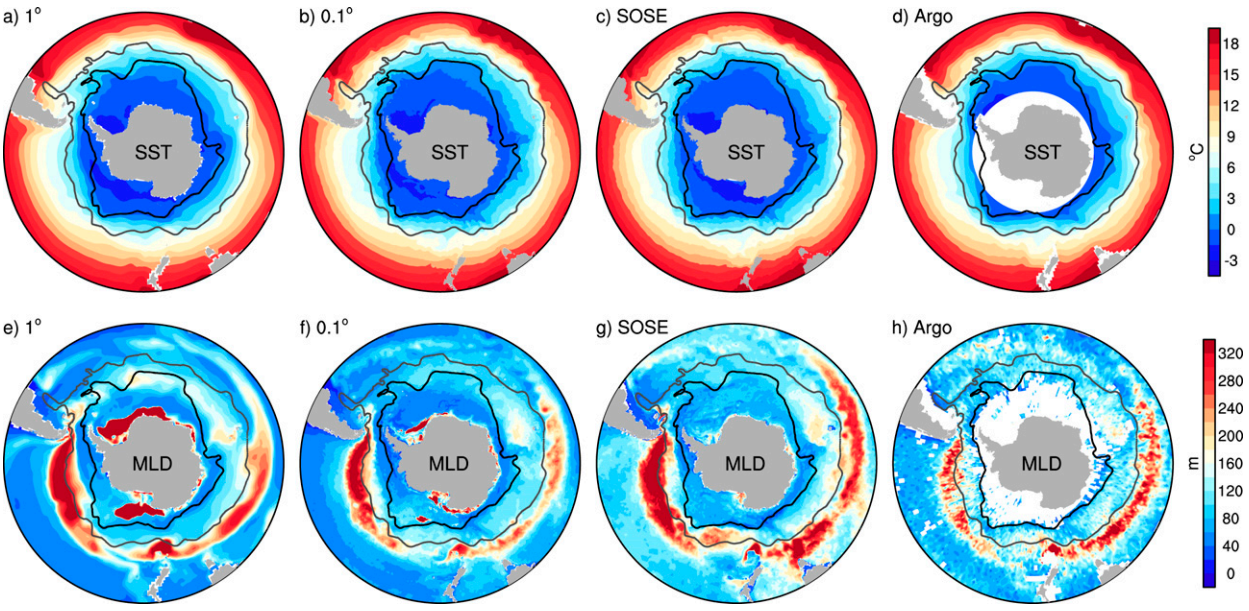

FIG. 1. (a)–(d) Annual-mean SST (°C; color) and (e)–(h) August–October mean MLD (m; color) from the model simulation at 1° and 0.1° resolution, SOSE and Argo data, respectively. Overlaid gray and black contours denote the Subantarctic Front (SAF) and Southern ACC Front (SACCF; Orsi et al. 1995), respectively.

ventilation (Abernathey and Ferreira 2015; Talley et al. 2016), which are less sensitive to the westerly wind shift in the Southern Ocean (Waugh et al. 2019).

Observations in the Southern Ocean have shown notable changes over the past few decades. For example, the surface Southern Ocean has cooled (Durack et al. 2012; Levitus et al. 2012; Armour et al. 2016; Swart et al. 2018) and freshened (Haumann et al. 2016; Swart et al. 2018), and overall sea ice has increased (Purich et al. 2016). This cooling is in stark contrast to the Arctic, which has seen rapid warming and sea ice retreat under anthropogenic climate change (Marshall et al. 2014). The increased Southern Ocean sea ice extent and surface cooling have been linked to glacial melt around Antarctica (Bintanja et al. 2013), sea ice feedbacks (Haumann et al. 2016, 2020), and enhanced northward Ekman transport of cool fresh Antarctic surface waters (Ferreira et al. 2015; Armour et al. 2016; Swart et al. 2018). In addition, surface freshening driven by sea ice changes (Kirkman and Bitz 2011; Haumann et al. 2016), glacial melt (Bintanja et al. 2013), and precipitation trends (Purich et al. 2018) can result in enhanced upper ocean stratification, which reduces convective mixing, leading to warmer subsurface waters. Indeed, recent observations reveal that subsurface waters have become warmer and saltier at these latitudes in the Southern Ocean (Gille 2002; Levitus et al. 2012; Swart et al. 2018). A long-term abyssal warming trend has also been detected in the Southern Ocean (Purkey and Johnson 2013), likely due to a combination of changes in dense shelf water properties and a reduction in the formation rates of cold Antarctic Bottom Water.

Modeling studies suggest that surface cooling across the Southern Ocean will eventually reverse due to direct surface warming by greenhouse gases as well as the eventual upwelling of warm Circumpolar Deep Water driven by a robust positive trend in the SAM (Marshall et al. 2014; Ferreira et al. 2015). The initial SST cooling phase occurs on interannual time scales driven by enhanced northward Ekman drift, but the delayed warming is much slower on the time scale of years to decades, referred to as "a two-time-scale problem" (Ferreira et al. 2015). However, exactly when the transition between the cooling and warming regimes will happen over the coming years or decades remains an open question. This uncertainty is partly because other factors at high latitudes also need to be considered, such as eddy effects (Doddridge et al. 2019), sea ice transport (Haumann et al. 2016), and glacial melt (Bintanja et al. 2013), and also because the time scale of transition is highly model-dependent (Ferreira et al. 2015; Kostov et al. 2017, 2018). Purich et al. (2016) suggest that due to an underestimate of summertime westerly wind intensification, climate models produce insufficient high-latitude surface cooling and sea ice increase. In addition, by using coarse-resolution ocean models, most previous studies cannot adequately capture the effect of mesoscale eddies on vertical mixing and the heat budget of the surface mixed layer (Griffies et al. 2015), also producing overly deep convection in certain regions of the Southern Ocean (Gent 2011).

The rate of SST warming in response to increased westerly winds depends on both the background meridional overturning circulation (MOC; Toggweiler and Russell 2008) as well as the near-surface vertical and lateral temperature gradients around Antarctica (Kostov et al. 2018), which are sensitive to the model resolution. The Southern Ocean MOC is a small residual between two opposing cells: the wind-driven Ekman circulation of the Deacon cell and the partially compensating eddy-driven circulation (Marshall and Radko 2003). With

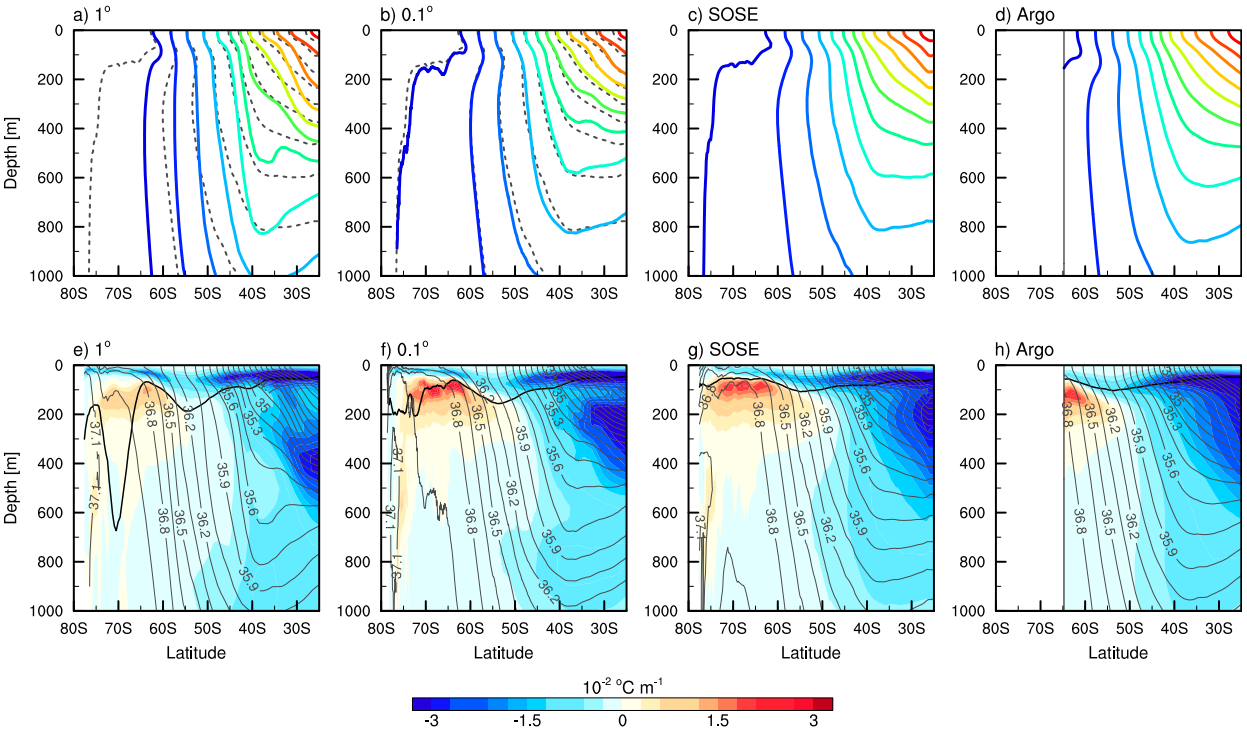

FIG. 2. Annual-mean and zonal-mean ocean Conservative Temperature (°C; contours) from the model simulation at (a) 1° and (b) 0.1° resolution, (c) ocean potential temperature (°C; contours) from SOSE, and (d) ocean temperature (°C; contours) from Argo data. Temperature ranges from −2° to 24°C with an interval of 2°C. Overlaid black dashed contours in (a) and (b) represent the potential temperature from SOSE as shown in (c). (e)–(h) The corresponding vertical gradient of temperature ($-\partial T/\partial z$; °C m^{-1}; color), density (kg m^{-3}; gray contours), and MLD (m; black line). The density was post calculated using the library of McDougall and Barker (2011), and it ranges from 33.5 to 37.1 kg m^{-3} with an interval of 0.15 kg m^{-3}. The vertical temperature inversion is indicated by $-\partial T/\partial z > 0$.

increasing wind, the changes in Ekman circulation across the ACC can be partially compensated by changes in eddy circulation, although the surface boundary conditions also have an impact on the degree of compensation (Abernathey et al. 2011). The increased Ekman upwelling and associated upward heat transport could also be compensated by mesoscale eddies (Doddridge et al. 2019). The Ekman response to the wind forcing is essentially instantaneous, but the time scale of eddy response is less clear. Meredith and Hogg (2006) suggested that the response time of surface eddies to the SAM is approximately 2 years. However, Treguier et al. (2010) argued that there is no SAM-linked trend in eddy compensation over a long-term scale.

In this study, we will investigate the time-dependent response of the Southern Ocean using a global ocean–sea ice model at both 1° and 0.1° resolutions. The coarser resolution typifies models used in the Coupled Model Intercomparison Projects (CMIPs), whereas the latter pushes the boundaries of modern-day computational systems. The model is forced by idealized perturbations that include the most significant wind and warming changes expected to occur over the Southern Hemisphere in the next few decades, namely increasing westerly winds and anthropogenic warming. The perturbation experiments are in particular geared toward understanding the potential upcoming changes across the Southern Ocean over the next few decades, rather than explaining the recent observed trends in SST and sea ice. The remainder of this paper is organized as follows. In section 2, the baseline model simulation and data are presented. In section 3, the experimental design is described. Sections 4 and 5 show the responses of Southern Ocean surface temperature and interior circulation to the perturbed forcing, respectively. Section 6 discusses the response of the model simulations in the SAMW formation regions north of the ACC. Finally, section 7 contains a summary and the conclusions of our study.

2. The baseline model simulation and data

a. *Model configurations*

This study uses the Australian Community Climate and Earth System Simulator Ocean Model version 2 (ACCESS-OM2) with configurations at two horizontal resolutions: ACCESS-OM2 (nominally 1° horizontal grid spacing) and ACCESS-OM2-01 (nominally 0.1° spacing). ACCESS-OM2 is a global ocean–sea ice model driven by a prescribed atmosphere (Kiss et al. 2020). The ocean model component is the Modular Ocean Model version 5.1 (MOM5.1; Griffies 2012), coupled to the Community Ice Code version 5.1.2 (CICE5.1.2; Hunke et al. 2015) sea ice component. The model experiment was forced with surface

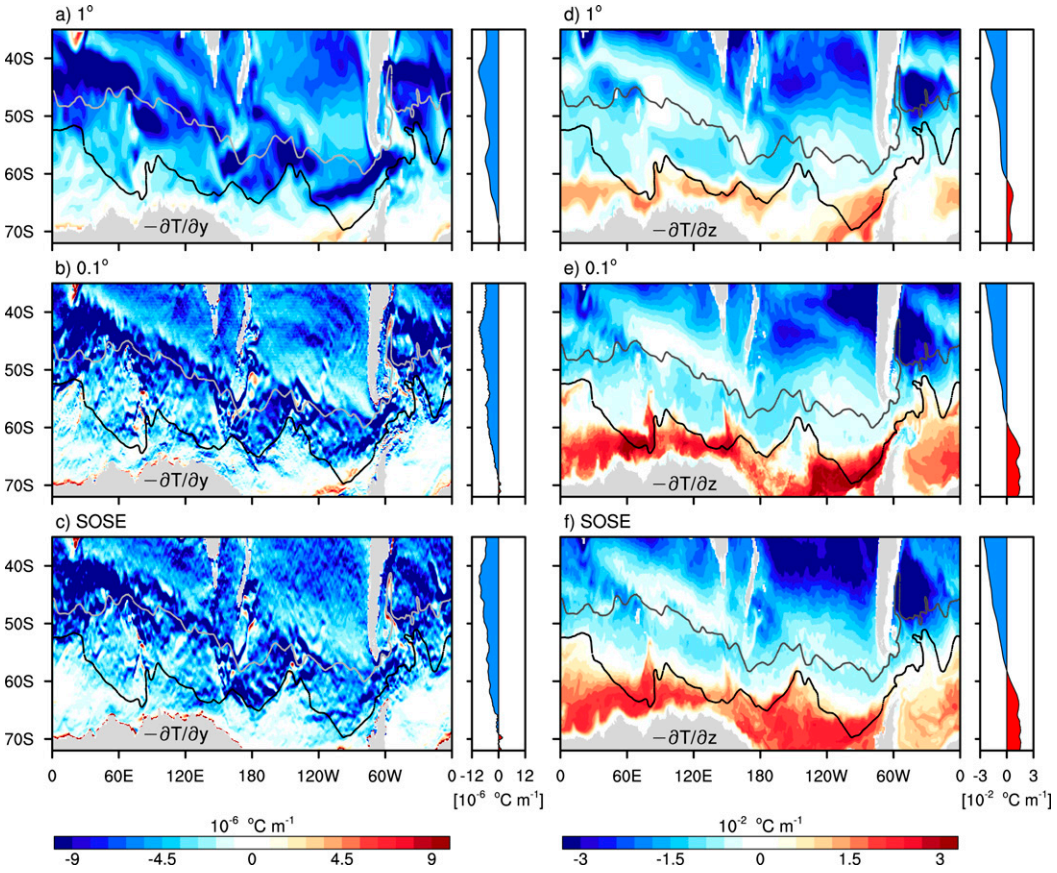

FIG. 3. Annual-mean (a)–(c) meridional gradient of SST ($-\partial T/\partial y$; °C m^{-1}; color) and (d)–(f) vertical temperature gradient between 150 and 40 m depth ($-\partial T/\partial z$; °C m^{-1}; color) from the model simulation at (top) 1° and (middle) 0.1° resolution, and (bottom) from SOSE. A zonal average plot is attached on the right panel for each subplot. Overlaid gray and black contours denote the SAF and SACCF (Orsi et al. 1995), respectively. The vertical temperature inversion is indicated by $-\partial T/\partial z > 0$.

atmospheric variables based on the Japanese 55-Year Reanalysis (JRA-55) dataset for driving ocean–sea ice models version 1.3 (hereafter referred to as JRA55-do v1.3; Tsujino et al. 2018). In all model simulations the atmospheric forcing is identical between the 1° and 0.1° runs; however, some differences can arise in the air–sea fluxes across resolutions wherever oceanic properties determine the magnitude of the flux (e.g., surface wind stress, outgoing longwave radiation, and sensible heat fluxes).

The two model configurations use a tripolar grid with one pole located at the South Pole and the other two poles located north of 65°N, and a Mercator projection down to 65°S. South of 65°S, the meridional grid spacing is held at the same value (in km) as 65°S. Both model configurations employ a z^* generalized vertical coordinate with partial cells, and they each include the boundary layer K-profile parameterization (KPP; Large et al. 1994) with a constant background vertical viscosity of 10^{-4} m^2 s^{-1}.

For the coarse-resolution ACCESS-OM2, the median zonal cell size is about 92 km globally. The vertical grid has 50 levels with grid spacing from 2.3 m at the surface to 219.6 m by the bottom at 5363.5 m. In this configuration, the Gent and McWilliams (GM) parameterization (Gent and McWilliams 1990; Gent et al. 1995) with the diffusivity limited to the ranges of 50–600 m^2 s^{-1} is used to represent the eddy tracer fluxes induced by mesoscale baroclinic turbulence. The Redi parameterization (Redi 1982) with a coefficient globally constant at 600 m^2 s^{-1} is used to represent unresolved isopycnal mixing of tracers.

For the high-resolution ACCESS-OM2-01, the median zonal cell size is about 7.2 km globally. In the Southern Ocean, the horizontal resolution ranges from 9 km at 36°S to 4 km at 68°S; hence, it is eddy-permitting in this region and resolves the largest baroclinic mesoscale eddies. The model uses a 75-level vertical grid with grid spacing from 1.1 m at the surface to 198.4 m by the bottom at 5808.7 m. There is no subgrid-scale parameterization for mesoscale eddies included in the eddy-rich ACCESS-OM2-01.

b. Temperature budget

The contribution of individual physical processes to the temperature changes across the Southern Ocean is examined in the temperature budget, expressed as

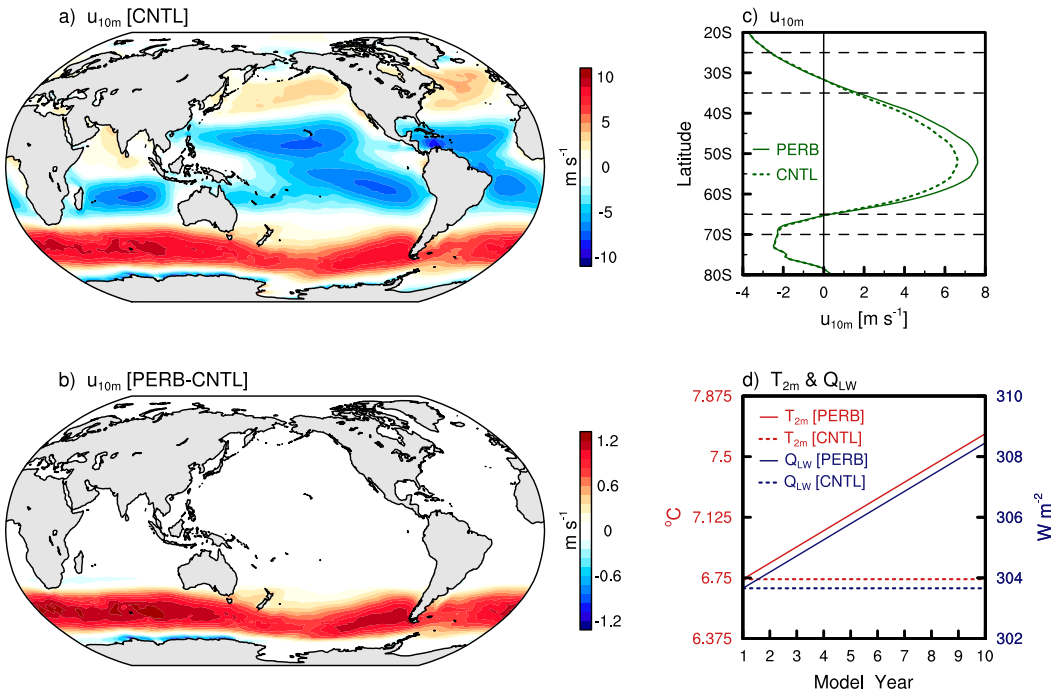

FIG. 4. (a) 10-m zonal wind velocity (u_{10m}; $m\,s^{-1}$) in the control experiment and (b) the u_{10m} difference ($m\,s^{-1}$) between the perturbation and control experiments. (c) Zonal-mean u_{10m} ($m\,s^{-1}$) in the control (dashed line) and perturbation (solid line) experiments. (d) Global-mean 2-m air temperature (T_{2m}; °C; red lines) and net surface longwave radiation (Q_{LW}; $W\,m^{-2}$; blue lines) in the control (dashed lines) and perturbation (solid lines) experiments.

$$\underbrace{\frac{\partial \Theta}{\partial t}}_{\text{temperature tendency}} = \underbrace{-\mathbf{u}\cdot\nabla\Theta}_{\text{advection}} \underbrace{-\frac{\partial}{\partial z}\overbrace{\left[-\kappa_Z\left(\frac{\partial \Theta}{\partial z}-\gamma_\Theta\right)\right]}^{\overline{w\Theta}}}_{\text{vertical mixing}} + \underbrace{\frac{1}{\rho c_w}\frac{\partial q}{\partial z}}_{\substack{\text{diabatic heating}\\ \text{from penetrative}\\ \text{shortwave flux}}} + \underbrace{\text{Res}}_{\substack{\text{other subgrid-scale}\\ \text{processes}}}, \tag{1}$$

with the boundary condition

$$\overline{w\Theta}_0 = \frac{Q_{\text{net}}}{\rho_0 c_w} \text{ at } z = 0,$$

where Θ is ocean conservative temperature, $\mathbf{u} = (u, v, w)$ is the three-dimensional current velocity, $\nabla = (\partial/\partial x, \partial/\partial y, \partial/\partial z)$ is the three-dimensional gradient operator, κ_z is the vertical diffusivity, γ_Θ is the nonlocal KPP transport of temperature, q is the penetrative shortwave flux (positive into the ocean) distributed vertically over several upper model layers, ρ is the density, c_w is the specific heat capacity of seawater, and Q_{net} is the net air–sea heat flux (from the atmosphere to the ocean is defined as positive). Due to the development of deep convection around Antarctica, we also separately diagnose the convective mixing term in Eq. (1) above, which is included in the vertical mixing. In response to the wind intensification, the meridional and vertical Ekman heat advection terms are also separately quantified.

c. Ocean state estimation and observation

The Southern Ocean State Estimation (SOSE) temperature and MLD output with eddy-permitting resolution at 1/6° × 1/6° for the time period of 2005–10 was also analyzed. The SOSE is an optimized fit to Southern Ocean observations while still obeying model physics (Mazloff et al. 2010). The 2004–18 mean temperature field at 1/6° × 1/6° resolution from the Argo data (Roemmich and Gilson 2009) was used in this study. The Argo-float-based MLD was estimated using a hybrid algorithm method (Holte et al. 2017) during 2000–19. The density based on both SOSE and Argo data was post calculated using the library of McDougall and Barker (2011).

d. Intermodel differences

The annual-mean SSTs from the model simulation at 1° and 0.1° resolution, SOSE, and Argo data are presented in Figs. 1a–d, respectively. The coverage of Argo data is poor south of 65°S. The increased horizontal resolution reveals more filamentary structure in the 0.1° SST field (Fig. 1b). Figures 1e and 1f respectively show the 1° and 0.1° winter (August-to-October mean) mixed layer depths (MLDs), which are defined based on a density criterion of $\Delta\sigma = 0.03\,kg\,m^{-3}$ (e.g., de Boyer Montégut et al. 2004). Compared with the 1° model, the mixed layers in the 0.1° simulation adjacent to the Subantarctic Front

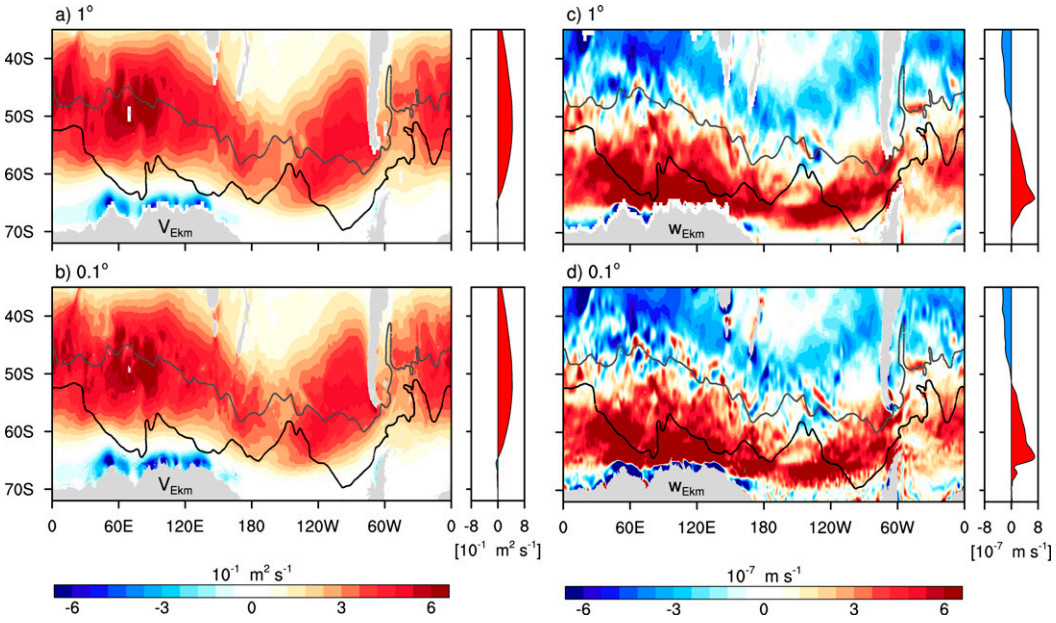

FIG. 5. The 10-yr mean (a),(b) meridional Ekman transport anomalies (V_{Ekm}; $\mathrm{m^2\,s^{-1}}$; color) and (c),(d) vertical Ekman velocity anomalies (w_{Ekm}; $\mathrm{m\,s^{-1}}$; color) from the model simulation at (top) 1° and (bottom) 0.1° resolution. A zonal average plot is attached on the right panel for each subplot. Overlaid gray and black contours denote the SAF and SACCF (Orsi et al. 1995), respectively.

(SAF) are relatively shallower and narrower in the meridional extent. The 0.1° MLD at midlatitudes is closer to the Argo-based MLD (Fig. 1h) because of its better representation of mesoscale eddies' contribution (Li and Lee 2017; Li et al. 2018). The 1° MLD bias at midlatitudes is related to spurious convection induced by insufficient dense water beneath the surface mixed layer. In contrast with the SOSE MLD (Fig. 1g), the 1° MLD bias at high latitudes is due to erroneous abyssal

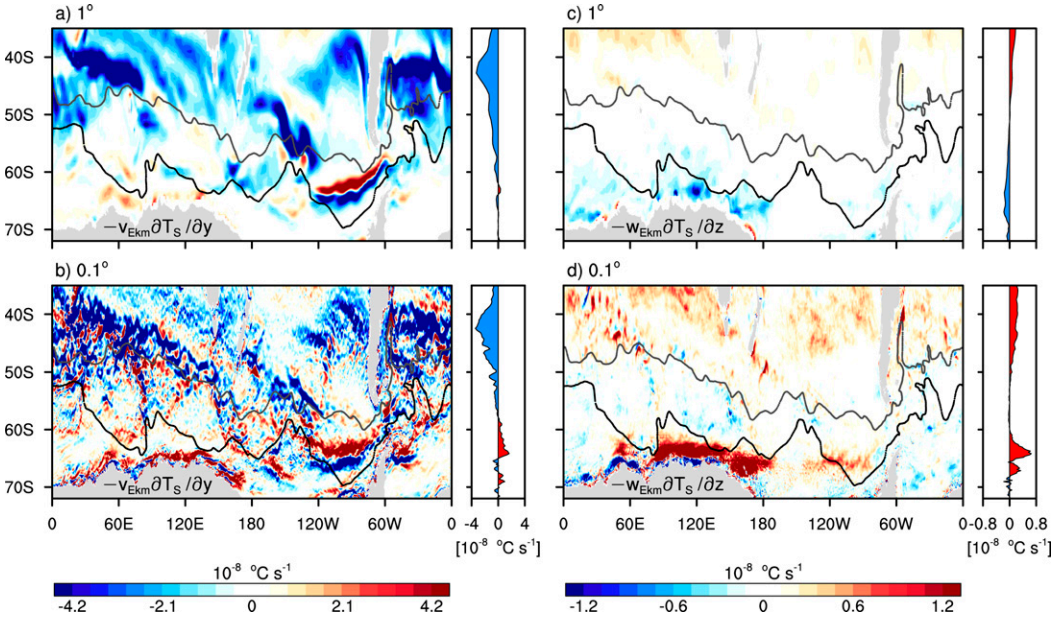

FIG. 6. The 10-yr mean (a),(b) meridional Ekman heat advection anomalies ($-v_{\mathrm{Ekm}}\partial T_s/\partial y$; $\mathrm{^\circ C\,s^{-1}}$; color) at the sea surface and (c),(d) vertical Ekman heat advection anomalies ($-w_{\mathrm{Ekm}}\partial T_s/\partial z$; $\mathrm{^\circ C\,s^{-1}}$; color) between the first two model levels from the model simulation at (top) 1° and (bottom) 0.1° resolution. A zonal average plot is attached on the right panel for each subplot. Overlaid gray and black contours denote the SAF and SACCF (Orsi et al. 1995), respectively.

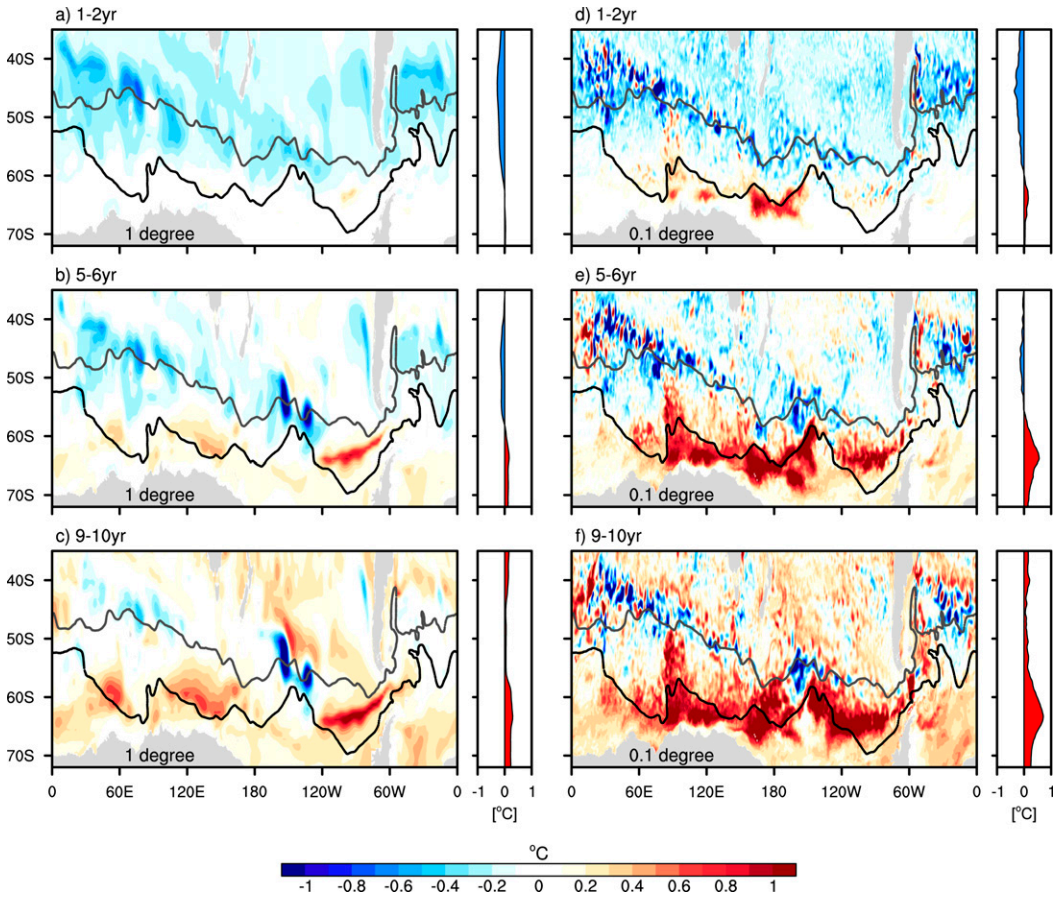

FIG. 7. SST anomalies (°C; color) averaged for years (a),(d) 1–2, (b),(e) 5–6, and (c),(f) 9–10 in the Southern Ocean from the model simulation at (left) 1° and (right) 0.1° resolution. A zonal average plot is attached on the right panel for each subplot. Overlaid gray and black contours denote the SAF and SACCF (Orsi et al. 1995), respectively.

water overturning occurring there, instead of over the Antarctic continental shelf.

In comparison with SOSE and Argo, the vertical distribution of zonal-mean ocean temperature is better represented in the 0.1° model than in the 1° model (Fig. 2). For example, isothermal surfaces are steeper at midlatitudes between 40° and 60°S in the 1° model (Fig. 2a), caused by its underrepresentation of the impact of mesoscale eddies on tracer advection (Jayne and Marotzke 2002; Gent 2011; Griffies et al. 2015). In contrast with SOSE, the 1° model shows a weaker near-surface vertical temperature inversion and resultant greater density at high latitudes between 60° and 75°S (Figs. 2a,e), because of its relatively coarse vertical resolution (Stewart and Hogg 2019). This temperature inversion governs the ocean stratification immediately below the MLD, which turns out to be critical for the ocean model response to wind changes over the Southern Ocean.

Figure 3 shows a further intermodel comparison of the meridional and vertical gradients of ocean temperature, which are two key factors of ocean heat transport. Again, more fine structure is present in the meridional temperature gradient in the 0.1° model (Fig. 3b) and SOSE (Fig. 3c) compared to the 1° model (Fig. 3a). The magnitude of the vertical temperature gradient around Antarctica at 0.1° is about $3 \times 10^{-2}\,°\mathrm{C\,m^{-1}}$ (Fig. 3e), similar to that in SOSE (Fig. 3f). In contrast, this vertical temperature inversion is much weaker ($\lesssim 1 \times 10^{-2}\,°\mathrm{C\,m^{-1}}$) in the 1° model (Fig. 3d).

3. Experimental design

Southern Hemisphere poleward-intensifying winds associated with a tendency of positive SAM phase have been directly influenced by Antarctic ozone depletion since around the 1960s (Thompson et al. 2011), which has also begun to show signs of recovery more recently (Solomon et al. 2016; Banerjee et al. 2020). Paleoclimate records from ice cores suggest that the westerly winds have been significantly increasing at a steady rate since 1940, and are currently the strongest they have been for at least the past 1000 years (Abram et al. 2014). Previous modeling studies have applied a step-change wind perturbation with an anomalous increase in the westerly winds to mimic ozone-hole forcing (Marshall et al. 2014; Bishop et al.

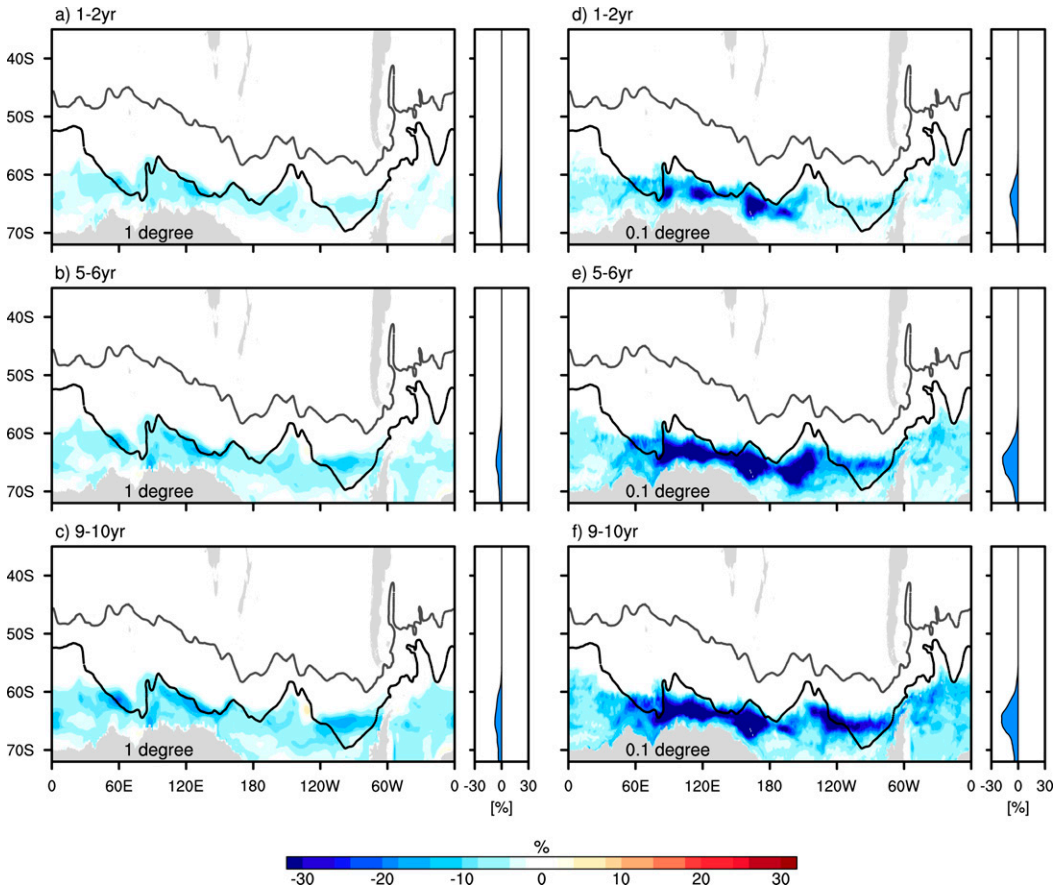

FIG. 8. Sea ice concentration anomalies (%; color) averaged for years (a),(d) 1–2, (b),(e) 5–6, and (c),(f) 9–10 in the Southern Ocean from the model simulation at (left) 1° and (right) 0.1° resolution, respectively. A zonal average plot is attached on the right panel for each subplot. Overlaid gray and black contours denote the SAF and SACCF (Orsi et al. 1995), respectively.

2016; Hogg et al. 2017). We also apply such a wind perturbation, and we extend previous work by combining the wind forcing with a thermal forcing applied to mimic greenhouse gas warming. Since the wind intensification associated with ozone depletion occurred earlier in the record than greenhouse gas warming (Polvani et al. 2011; Waugh et al. 2015), the wind forcing is designed with a step function as used in previous studies, whereas the thermal forcing is added gradually with a linear function of time in the perturbation experiment. Further details about experimental design are provided below.

The ACCESS-OM2 and ACCESS-OM2-01 were spun up for 200 and 120 years, respectively. Following the spinup, the control and perturbation experiments were each run for 10 years for both models. The spinup and control experiments were forced by JRA55-do v1.3 using the May 1990–April 1991 repeat-year forcing (Stewart et al. 2020). The anomalies between concurrent periods of the perturbation and control experiments are analyzed to minimize the influence of model drift on our results.

The wind perturbation was conducted by multiplying the 10-m zonal wind velocity by 1.15 south of 35°S, with this factor linearly tapered to 1 to the north between 35° and 25°S and to the south between 65° and 70°S (Figs. 4a–c). As a result, the Southern Hemisphere westerly winds are increased in magnitude by 15%, which corresponds to an increase of ~35% in the peak zonal wind stress. There is also a small increase in the coastal easterlies around East Antarctica (Fig. 4b).

The thermal perturbation was applied globally, with a linear increase of 0.1°C yr^{-1} in 2-m air temperature (T_{2m}) and a linear increase of 0.53 W m^{-2} yr^{-1} in net surface downwelling longwave radiation (Q_{LW}), as shown in Fig. 4d. Following the representative concentration pathway 4.5 (RCP4.5) scenario under moderate greenhouse gas emissions, the total increases are 1°C in T_{2m} and 5.3 W m^{-2} yr^{-1} in Q_{LW} at the end of the model simulation period of 10 years, as suggested in Snow et al. (2015).

4. Southern Ocean surface response

a. Role of Ekman heat advection

A step increase in wind generates a nearly instantaneous response of meridional Ekman transport (V_{Ekm}) and vertical Ekman velocity (w_{Ekm}), expressed as

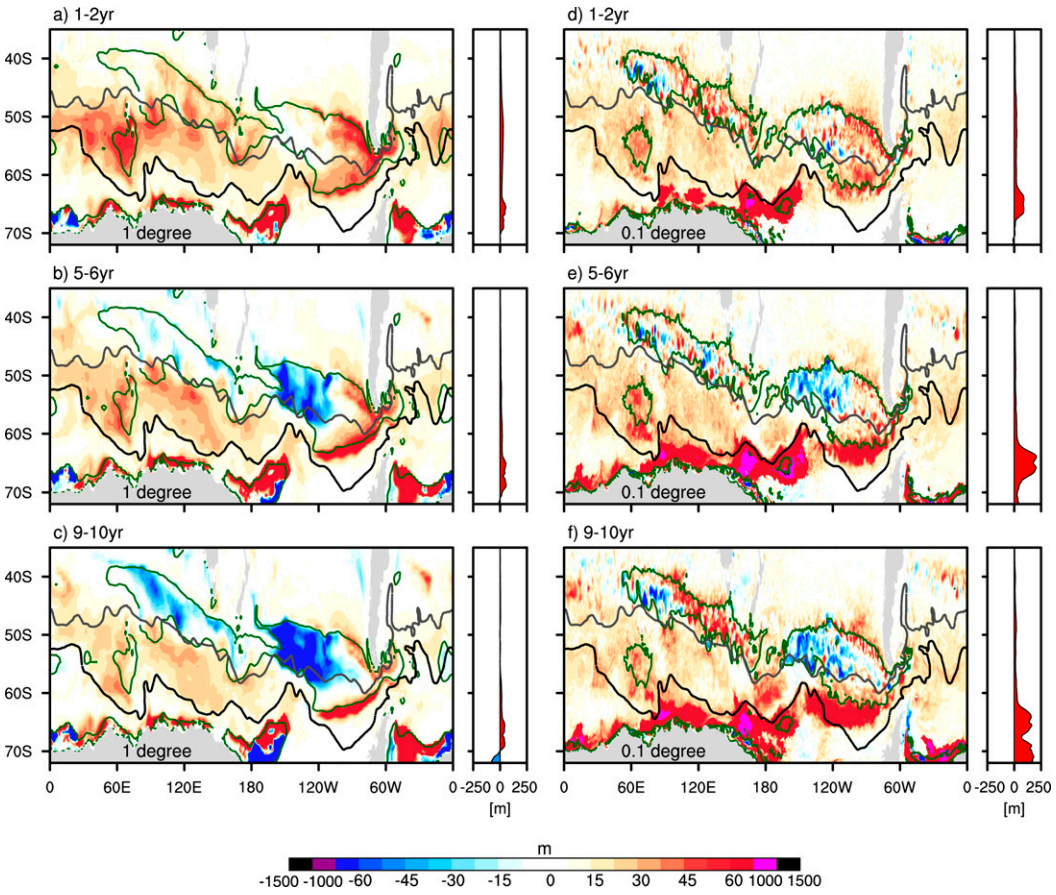

FIG. 9. MLD anomalies (m; color) averaged for years (a),(d) 1–2, (b),(e) 5–6, and (c),(f) 9–10 in the Southern Ocean from the model simulation at (left) 1° and (right) 0.1° resolution. Green contours indicate the annual-mean 150-m MLD from the control experiment. A zonal average plot is attached on the right panel for each subplot. Overlaid gray and black contours denote the SAF and SACCF (Orsi et al. 1995), respectively.

$$\begin{cases} V_{\mathrm{Ekm}} = -\dfrac{\tau_x}{\rho_0 f} \\ w_{\mathrm{Ekm}} = \dfrac{1}{\rho_0}\left(\dfrac{\partial}{\partial x}\dfrac{\tau_y}{f} - \dfrac{\partial}{\partial y}\dfrac{\tau_x}{f}\right) \end{cases},$$

where τ_x and τ_y are the zonal and meridional total surface stress, respectively; $\rho_0 = 1035\,\mathrm{kg\,m^{-3}}$ is a reference density; $f = 2\omega\sin(\phi)$ is the Coriolis parameter, ω is the angular velocity of Earth's rotation, and ϕ is the latitude. Because we applied the repeat-year forcing, Ekman velocities have little year-to-year variation. In addition, changes in Ekman velocities are largely insensitive to the model resolution (Fig. 5). In both models, there is a significant circumpolar increase in the meridional Ekman transport anomalies at midlatitudes (Figs. 5a and 5b). The vertical Ekman velocity anomalies also exhibit a circumpolar signature with a decrease (anomalous downwelling) to the north and an increase (anomalous upwelling) to the south. The anomalous upwelling is distributed between the Southern ACC Front (SACCF) and Antarctica (Figs. 5c,d).

We next use the diagnosed Ekman velocities and temperature gradients to estimate the changes in surface meridional Ekman heat advection ($-v_{\mathrm{Ekm}}\partial T_s/\partial y$) and vertical Ekman heat advection ($-w_{\mathrm{Ekm}}\partial T_s/\partial z$), where $v = V_{\mathrm{Ekm}}/h_m$, and h_m is the depth of mixed layer; while $-\partial T_s/\partial y$ is the meridional gradient of temperature at the sea surface, and $-\partial T_s/\partial z$ is the vertical gradient of temperature between the first two model levels. There is clear evidence that both types of Ekman heat advection depend on model resolution (Fig. 6). This model dependence is mainly because of fine structures in the gradients of temperature, $-\partial T_s/\partial y$ and $-\partial T_s/\partial z$.

The meridional Ekman heat advection is anomalously negative between 35° and 60°S (Figs. 6a,b) due to increased northward transport of relatively cold water by anomalous Ekman currents (Figs. 5a,b). Although the zonal-mean meridional Ekman heat advection anomalies at 1° and 0.1° are comparable, with a magnitude of $\sim 3 \times 10^{-8}\,^{\circ}\mathrm{C\,s^{-1}}$, there are more mesoscale eddying features in the 0.1° case, particularly along the path of the ACC (Fig. 6b). In addition, the 0.1° meridional heat advection south of 60°S shows large positive anomalies (Fig. 6b).

The vertical Ekman heat advection is anomalously positive north of 50°S (Figs. 6c,d) associated with increased downward

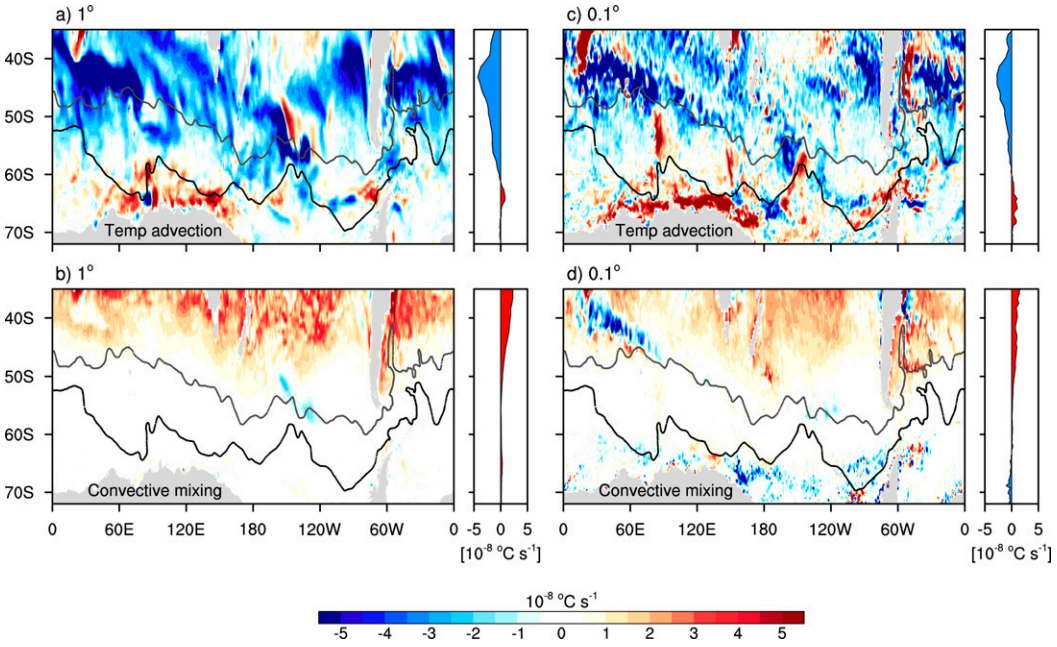

FIG. 10. The 10-yr mean mixed layer temperature tendency anomalies contributed from (a),(c) temperature advection and (b),(d) convective mixing (°C s^{-1}; color) from the model simulation at (top) 1° and (bottom) 0.1° resolution, respectively. A zonal average plot is attached on the right panel for each subplot. Overlaid gray and black contours denote the SAF and SACCF (Orsi et al. 1995), respectively.

transport of relatively warm surface water by anomalous Ekman downwelling (Figs. 5c,d). This warm vertical heat advection in the 0.1° case is larger, which is due to the more negative $-\partial T_s/\partial z$. Although the Ekman upwelling anomalies are nearly identical south of 60°S, there is a striking difference in the vertical Ekman heat advection between the 1° and 0.1° cases. The 0.1° vertical heat advection around East Antarctica and in the Ross Sea shows positive anomalies larger than 1×10^{-8} °C s^{-1} (Fig. 6d), which corresponds to positive $-\partial T_s/\partial z$. In contrast, due to the lack of this vertical temperature inversion ($-\partial T_s/\partial z < 0$) at coarse model resolution, the 1° vertical heat advection is anomalously negative in that region (Fig. 6c). This diagnostic implies that the 1° and 0.1° resolution models will actually have an opposite sign response to similar wind stress anomalies in this region.

b. *Transient surface response*

The Southern Ocean SST shows a robust time-dependent and model-dependent response to the perturbed wind and linearly-increased thermal forcing (Fig. 7). During years 1–2, the SST cools between 35° and 60°S (Figs. 7a,d), which is due to increased negative northward Ekman advection (Figs. 6a,b) as discussed in Rintoul and England (2002). In the 0.1° case, the cooling anomalies along the SAF are slightly stronger and the warming anomalies around East Antarctica and in the Ross Sea appear earlier (Fig. 7d) than those in the 1° case (Fig. 7a). Because of the overall weaker thermal forcing at the start of the run, the wind-driven cooling dominates the SST response early on. With the progressive increase in thermal forcing, a clear transition from a cooling phase to a warming phase takes place during years 5–6 (Figs. 7b,e). The SST anomalies show a pronounced increase (>1°C) south of the SACCF (Fig. 7e), where both the near-surface vertical temperature inversion and anomalous Ekman upwelling occur concurrently. When the perturbed surface heating has the greatest increase during years 9–10, the SST anomalies are dominated by widespread warming over most regions of the Southern Ocean, whereas a slight cooling remains along the SAF (Figs. 7c,f). Although both models can simulate this transition, stronger anomalous SST warming initiates and spreads northward in the 0.1° case (Figs. 7d–f).

Changes in SST south of the SACCF play an important role in sea ice fluctuations. During years 1–10 the sea ice concentration is continuously decreasing (Fig. 8), which is consistent with the SST warming anomalies around Antarctica (Fig. 7). Furthermore, a stronger decrease in sea ice in the 0.1° case can be seen, particularly around East Antarctica and in the Ross Sea (Figs. 8d–f), relative to the 1° case (Figs. 8a–c). This dramatically decreased sea ice further causes a significant increase in net incoming shortwave radiation (Qu and Hall 2005). Notably, the changes in sea ice concentration and SST south of 60°S are largely opposite to Ferreira et al. (2015), although in their simulations the shortwave absorption is reduced in spring to mimic ozone depletion effects, something that we do not include given that our focus is on the expected effects of wind and warming trends across the Southern Ocean over the next few decades.

The Southern Ocean MLD at midlatitudes has opposing responses to wind and thermal forcing. Initially, with the increasing wind, the MLD deepens rapidly due to enhanced

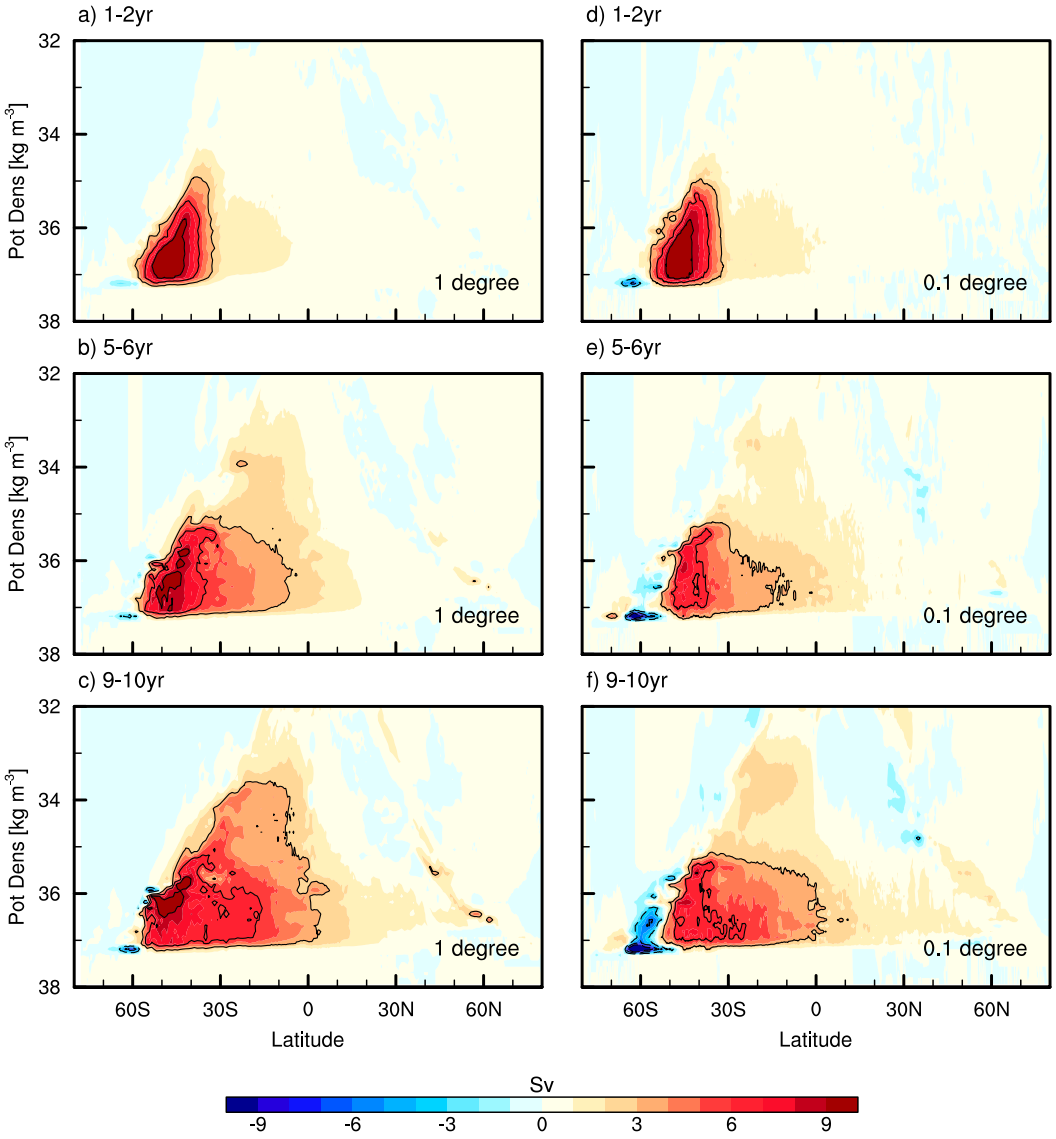

FIG. 11. Residual MOC anomalies (Sv) averaged for years (a),(d) 1–2, (b),(e) 5–6, and (c),(f) 9–10 from the model simulation at (left) 1° and (right) 0.1° resolution. Contours range from −9 to 9 Sv with an interval of 3 Sv.

vertical mixing and enhanced northward transport of cold, fresh, and dense Antarctic surface water (e.g., Rintoul and England 2002). At the early stage of years 1–2, the MLD anomalies show an increase of ~40 m at midlatitudes (Figs. 9a,d). Then later, with the increase in thermal forcing, the MLD tends to shoal due to enhanced upper ocean stratification (Panassa et al. 2018). During years 5–10, the MLD anomalies decrease in some locations at midlatitudes where the climatological mixed layers are deep (Figs. 9b,c,e,f). Notably, the midlatitude MLD response is more sensitive to the forcing in the 1° case than the 0.1° case. For example, the 1° MLD at midlatitudes exhibits greater increases during years 1–2 (Figs. 9a,d) and greater decreases during years 5–10 (Figs. 9b,c,e,f). A closer look at the 0.1° MLD anomalies during years 9–10 reveals that there is a significant increase along the northern flank of the SAF at 90°E–180° and 120°–60°W (Fig. 9f), which can facilitate enhanced subduction of warm surface water into the ocean interior (Gille 2002).

Furthermore, some MLD anomalies of 60–1000 m develop around Antarctica in the 0.1° case (Figs. 9d–f). This MLD deepening is coincident with anomalously warm mixed layer temperature advection (Fig. 10c), which results largely from upward Ekman heat advection (Fig. 6d). As noted earlier, around the Antarctic margin, a vertical temperature inversion occurs immediately below the climatological MLD (Fig. 2f). Through anomalous upward heat transport across the base of the mixed layer, this can trigger destratification and an increase in MLD. In the 0.1° case, a localized region of deep convection occurs around 163°E, where the mixed layer convective mixing shows small cooling anomalies (Fig. 10d). However, the MLD budget aliases convective overturn effects, which homogenize the water column

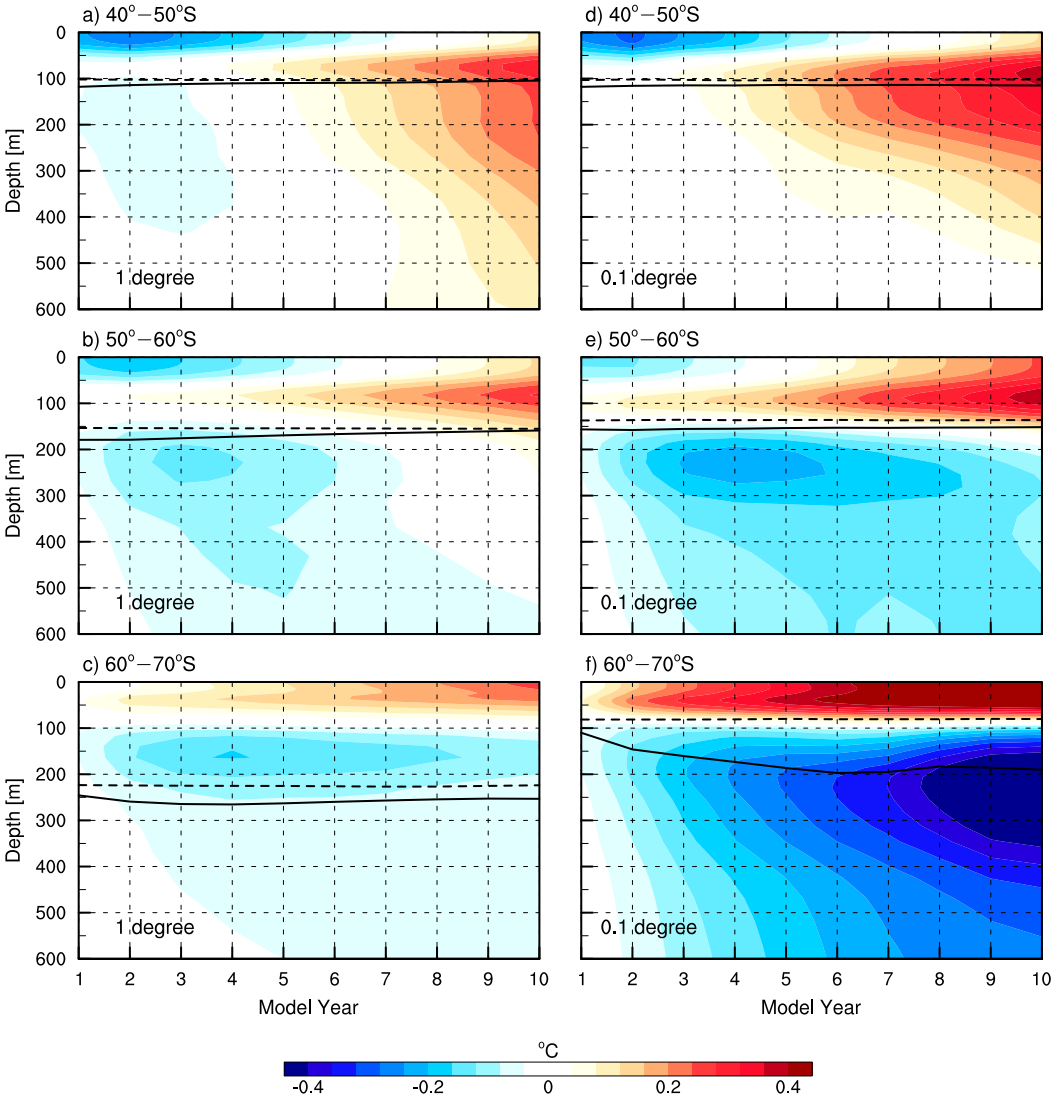

FIG. 12. Hovmöller diagram of zonal-mean ocean temperature anomalies at depths (°C; color) along three latitudinal bands of (a),(d) 40°–50°S, (b),(e) 50°–60°S, and (c),(f) 60°–70°S in the Southern Ocean from the model simulation at (left) 1° and (right) 0.1° resolution. Overlaid dashed and solid black lines represent the actual MLD (m) simulated from the control and perturbation experiment, respectively.

by inducing warming in the upper water column and cooling at depth. To more clearly diagnose convective overturning effects on upper-ocean temperatures, a heat budget for the upper 150 m is also diagnosed, as will be discussed later in the paper.

5. Ocean interior response

a. Residual MOC response

The residual MOC ($\psi_{\rm moc}$) is distributed along isopycnal surfaces and is thus calculated in latitude–density space (Döös and Webb 1994) as

$$\psi_{\rm moc}(y,\sigma) = \overline{\oint\int_{\sigma}^{\sigma_s} v h d\sigma' \, dx},$$

where v is the meridional velocity; $h(x, y, \sigma, t) \equiv -\partial\tilde{z}/\partial\sigma$ is the thickness of isopycnal layers, and $\tilde{z}$ is the depth of isopycnal surfaces; σ_s is the surface density, and σ is the potential density; x and y are the zonal and meridional coordinates, respectively; the overbar indicates a time average, $\overline{()} \equiv (1/\tau)\int_0^\tau () \, dt$, and τ is the averaging period. The response of the residual MOC to the perturbed forcing is presented in Fig. 11. Because of enhanced wind-driven circulation, we see that the increase in the residual MOC anomalies of greater than 9 Sv ($1\,{\rm Sv} \equiv 10^6\,{\rm m^3\,s^{-1}}$) is largest across the ACC between 30° and 60°S during years 1–2 in both models (Figs. 11a,d). The enhanced wind-driven circulation can only be partially compensated by parameterized eddy-driven circulation in the 1° model, due to its underrepresentation of mesoscale eddy impact on tracer advection

(Jayne and Marotzke 2002; Gent 2011; Griffies et al. 2015). This underrepresentation results in an increase of ~8 Sv in the residual MOC anomalies at 1° resolution during years 5–6 (Fig. 11b). In contrast, the 0.1° model can represent the effect of eddy compensation, which appears to occur over a time scale of ~5 years. Thus, there is a smaller increase (<5 Sv) in the residual MOC anomalies at 0.1° during years 5–6 (Fig. 11e). During years 9–10, the anomalous residual MOC further extends to the Northern Hemisphere via an acceleration of the Atlantic MOC (Figs. 11c,f). For the 0.1° case, an anomalous deep cell between 55° and 65° also develops (Fig. 11f), corresponding to an anomalous increase in MLD around Antarctica (Fig. 9f).

b. *Ocean temperature response*

Figure 12 shows the evolution of ocean interior temperature along three different latitudinal bands. Within the band 40°–50°S, the upper ocean above the MLD at ~100 m exhibits the greatest cooling anomalies, with a minimum value of about −0.3°C at year 2 in both models (Figs. 12a,d). This latitude band is a region of significant ocean ventilation, fed by northward Ekman transport, surface ocean heat loss, and subsequent SAMW convective overturn and subduction, so we may expect significant changes to accumulate there. Indeed, the subsurface water at both 1° and 0.1° shows remarkable warming anomalies of about 0.4°C at 100-m depth by year 10. The heat subduction penetrates to a depth of 600 m in the 1° case (Fig. 12a), although it remains stronger in the 0.1° case (Fig. 12d). In the latitudinal band 50°–60°S, there is a clear SST transition from cooling phase to warming phase (Figs. 12b,e). The time scale of this transition is ~7 years in the 1° case (Fig. 12b), whereas it is only ~5 years in the 0.1° case (Fig. 12e). Within the southernmost latitudinal band 60°–70°S, there is a vertical dipole pattern with warming above cooling in the temperature anomalies (Figs. 12c,f). A stronger dipole pattern develops in the 0.1° case, which is closely related to an increase in the MLD of ~100 m (Fig. 12f). As noted earlier, the enhanced upward Ekman heat advection initiates the mixed layer deepening around Antarctica, which corresponds to a decrease in sea ice and an increase in net incoming shortwave radiation. These increased upward Ekman heat advection and shortwave radiation are both responsible for the warming anomalies above 100 m. Instead, the cooling anomalies underneath are due to the increased removal of heat from vertical Ekman advection and the increased vertical mixing of colder waters at the base of the mixed layer.

6. SAMW formation

The key pathway of heat transport and sequestration in the Southern Ocean is through SAMW (Roemmich et al. 2015), characterized by a layer of highly oxygenated and weakly stratified water (Hanawa and Talley 2001). SAMW can be identified using potential vorticity (PV), defined as

$$\mathrm{PV} = \frac{f}{\sigma}\frac{\partial \sigma}{\partial z}.$$

The spatial distribution of SAMW with its low PV signature, simulated in the control experiments and SOSE, is presented in

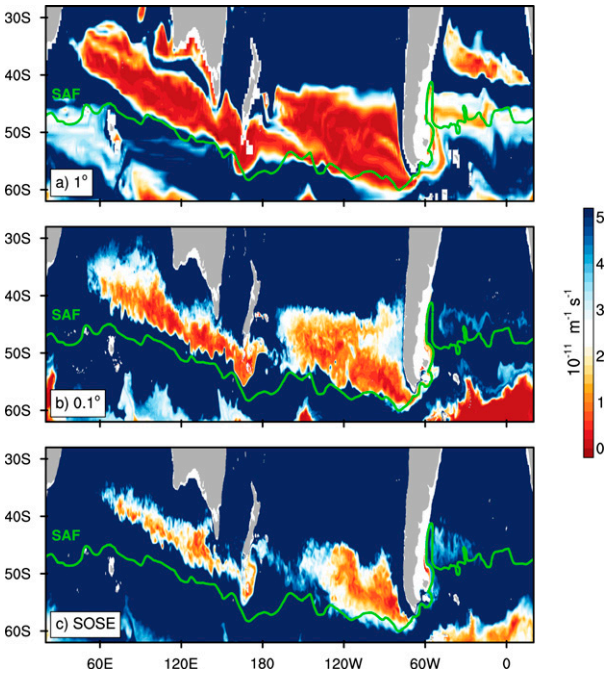

FIG. 13. Potential vorticity (PV; $\mathrm{m}^{-1}\,\mathrm{s}^{-1}$; color) at 300-m depth in June simulated from the control experiment at (a) 1° and (b) 0.1° resolution, and from (c) SOSE. Local minimum PV values indicate the SAMW formation regions. Overlaid green contours denote the SAF (Orsi et al. 1995).

Fig. 13. SAMW is generally found on the northern flank of the SAF (McCartney 1977). The meridional extent of SAMW in both the 0.1° model (Fig. 13b) and SOSE (Fig. 13c) is much narrower than in the 1° model (Fig. 13a).

SAMW originates in deep wintertime mixed layers, from where it is subducted and advected northward carrying its temperature/salinity properties, particularly in the southeast Pacific basin (Fig. 13; Sloyan and Rintoul 2001; Rintoul and England 2002; Downes et al. 2011). Therefore, we next investigate the response of isopycnal surfaces and temperature in the southeast Pacific to the forcing perturbation (Fig. 14). The increased wind and thermal forcing cause an enhanced ocean ventilation in the Southern Ocean, via the "pure warming subduction" and "pure heaving" mechanisms discussed in Bindoff and Mcdougall (1994).

The increasing wind also acts as a mechanical force to tilt isopycnal surfaces, which gives rise to an increase in available potential energy across the ACC. At the early stage of years 1–6, the subduction of surface water, associated with SAMW formation, follows the anomalously strong tilted isopycnals between 30° and 45°S in both models (Figs. 14a,b,d,e). In the 1° case, deep convection is further developed in the climatologically deep MLD region between 45° and 55°S during years 9–10. This anomalous deep convection leads to an even stronger steepening of isopycnal surfaces, resulting in a larger amount of heat subduction at that location (Fig. 14c). In contrast, although the anomalous subduction of surface water is also strengthened, it reorients to more closely follow isopycnal layers north of 45°S in the 0.1° case (Fig. 14f). Again, a stronger

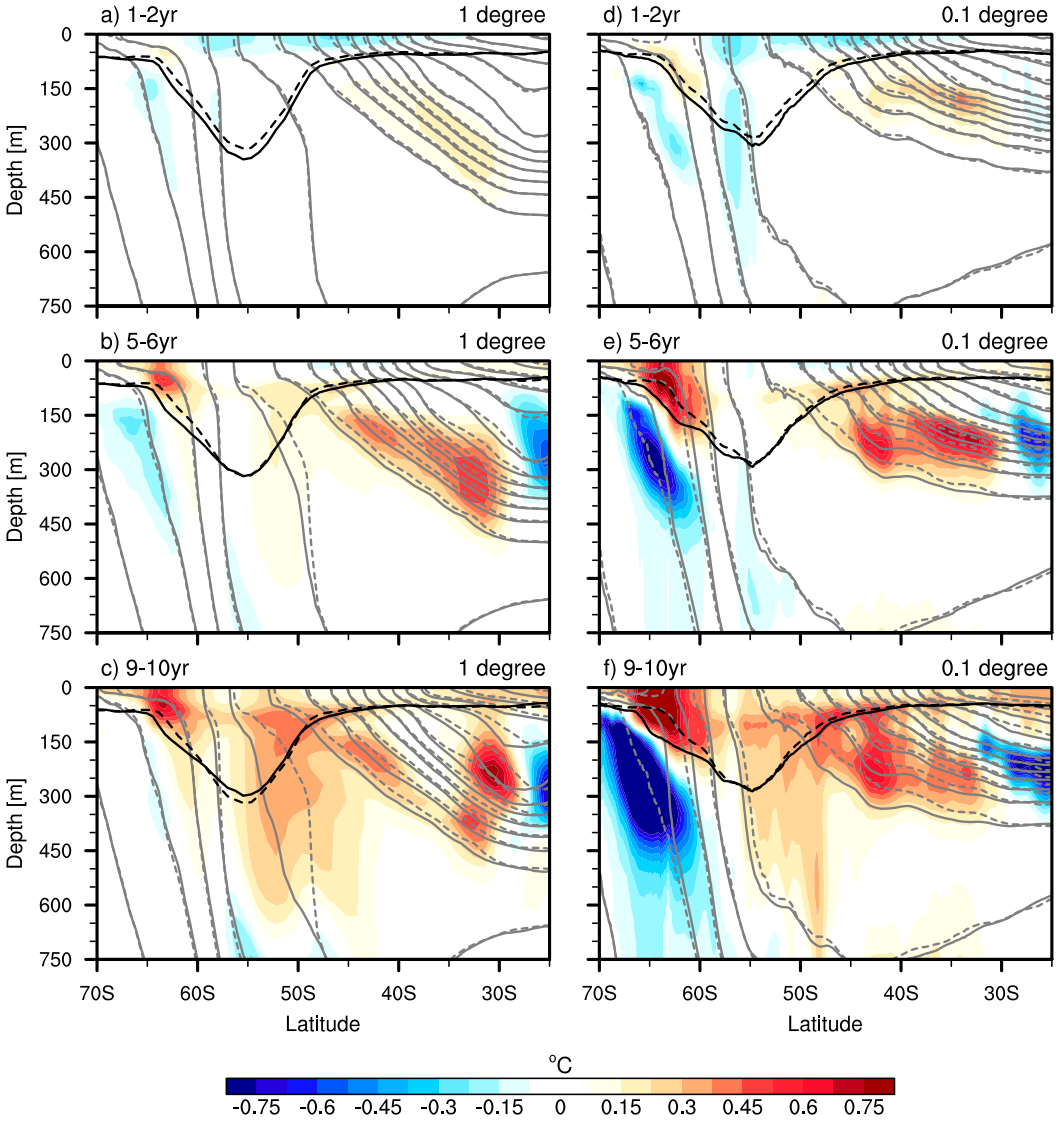

FIG. 14. Vertical cross section of zonal-mean ocean temperature anomalies (°C; color) averaged for years (a),(d) 1–2, (b),(e) 5–6, and (c),(f) 9–10 in the southeast Pacific (60°–130°W) from the model simulation at (left) 1° and (right) 0.1° resolution. Overlaid dashed and solid gray contours represent the actual potential density (kg m^{-3}) simulated from the control and perturbation experiment, respectively. The contour interval is 0.25 kg m^{-3}. Overlaid dashed and solid black lines represent the actual MLD (m) simulated from the control and perturbation experiment, respectively.

vertical dipole pattern of temperature anomalies is found south of 60°S in the 0.1° case (Figs. 14e,f).

7. Conclusions and discussion

Recent anthropogenic change in the Southern Hemisphere has resulted in a strengthening of the circumpolar westerly wind belt and enhanced radiative warming due to the greenhouse effect. These changes are expected to continue over the coming decades. To explore these factors, we analyzed the response of the Southern Ocean to idealized wind and heating perturbations using a global ocean–sea ice model at two horizontal resolutions: nominally, 1° and 0.1°. The SST shows a transient response with initial cooling north of 60°S, eventually overwhelmed by warming. South of 60°S, there is a tendency for more rapid warming around Antarctica (Figs. 15a,b) due to the near-surface vertical temperature inversion there. These SST variations are largely attributed to meridional and vertical Ekman heat advection, which are both sensitive to the model resolution. By comparison, the widespread SST warming occurs more strongly and rapidly in the 0.1° case with a transition period of ~2 years earlier relative to the 1° case.

The ocean's interior is also anomalously ventilated through enhanced subduction. Consistent with Armour et al. (2016),

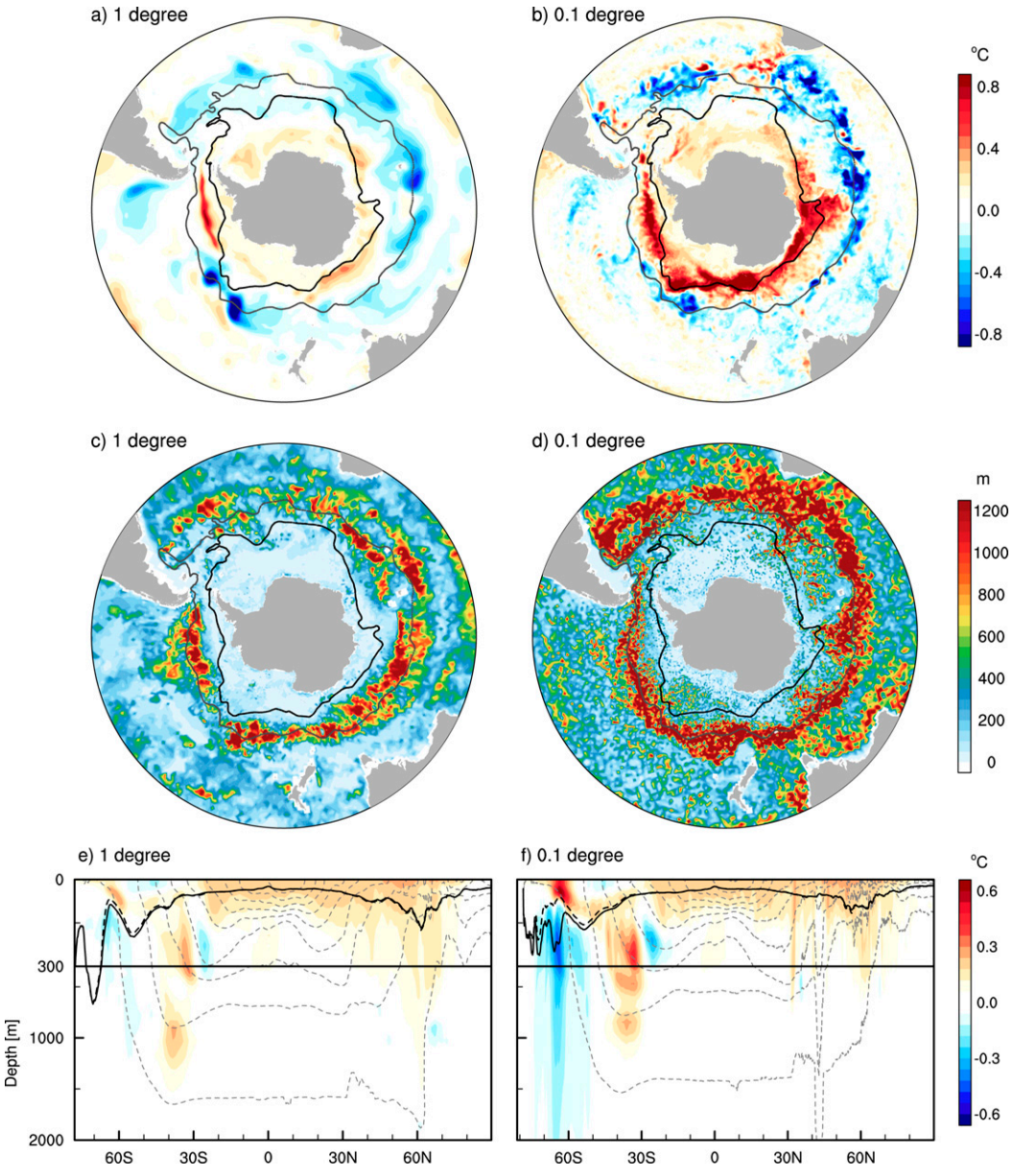

FIG. 15. The 10-yr mean (a),(b) SST anomalies (°C; color), (c),(d) depth of heat subduction (m; color) in the Southern Ocean, and (e),(f) zonal-mean ocean temperature anomalies at depths (°C; color) from the model simulation at (left) 1° and (right) 0.1° resolution. The depth of heat subduction is defined as the depth where temperature tendency first changes sign from positive to negative. Overlaid gray and black contours in (a) and (b) denote the SAF and SACCF (Orsi et al. 1995), respectively. Overlaid dashed gray contours in (c) and (d) represent the actual potential density (kg m^{-3}) simulated from the control experiment. The contour interval is 0.75 kg m^{-3}. Overlaid dashed and solid black lines in (c) and (d) represent the actual MLD (m) simulated from the control and perturbation experiment, respectively.

the heat subduction extends to depths greater than 1200 m on the northern flank of the ACC (Figs. 15c,d), which is closely tied to SAMW formation (Rintoul and England 2002). In the 0.1° case, the deepest heat subduction with a narrow meridional scale is located just north of the SAF (Fig. 15d). This fine structure on the oceanic jet scales is appreciably more accurate in high-resolution ocean model simulations than in simulations at coarser resolution, as per the mechanisms discussed in Li and Lee (2017). By further comparison, the 1° case reveals increased subduction via enhanced deep convection associated with more strongly steepened isopycnal surfaces at midlatitudes (Figs. 14c and 15e), which results from an enhanced wind-driven overturning, with only limited parameterized eddy-driven compensation. However, the 0.1° anomalous subduction is oriented more

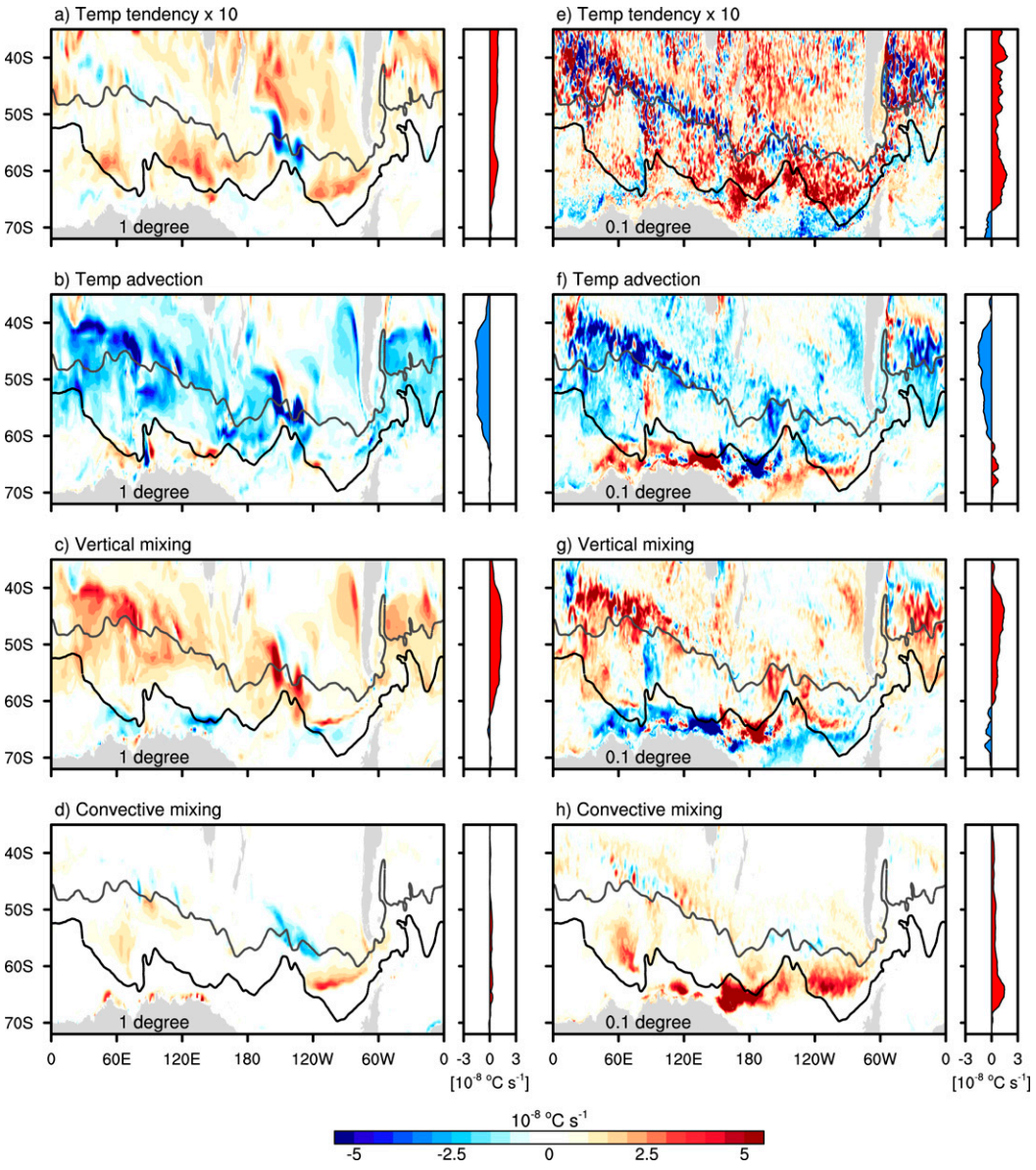

FIG. 16. The 10-yr mean upper-ocean (a),(e) temperature tendency anomalies and their contributions from (b),(f) temperature advection, (c),(g) vertical mixing, and (d),(h) convective mixing (°C s^{-1}; color) for the vertically weighted average in the upper ~150 m from the model simulation at (left) 1° and (right) 0.1° resolution, respectively. All the anomalies are vertically integrated from the model top level to the depth of ~150 m. A zonal average plot is attached on the right panel for each subplot. Overlaid gray and black contours denote the SAF and SACCF (Orsi et al. 1995), respectively.

along the isopycnals in the regions of SAMW formation (Figs. 14f and 15f). At high latitudes, the 0.1° case reveals a stronger vertical dipole pattern of temperature anomalies, with warming superimposed on cooling (Fig. 15f). Furthermore, within the model simulation period of 10 years, both cases show that the heat redistribution in the ocean interior further extends to the Northern Hemisphere via an acceleration of the Atlantic MOC.

With increased radiative heating, the warming response of the Southern Ocean occurs largely in the upper ~150 m, where the temperature budget is further examined. Consistent with the vertical advection–diffusion balance (Huber et al. 2015), the anomalous temperature tendency is only a residual between two dominant and opposing contributors: temperature advection and vertical mixing (Figs. 16a–c,e–g). Because the higher-resolution model at 0.1° has the ability to more accurately represent the pronounced near-surface vertical temperature inversion around Antarctica, a larger amount of warm temperature advection driven by anomalous Ekman upwelling is

found there (Fig. 16f). In compensation for the upward temperature advection, the vertical mixing causes a transport of heat from the upper ocean to the waters below, and thus causes cooling in the upper ocean (Fig. 16g). However, an exception occurs in a localized region over the Ross Sea, where the cooling anomalies are due to temperature advection (Fig. 16f) and the warming anomalies due to convective mixing (Fig. 16h). Once the convective overturn generates these warming anomalies, vertical diffusion acts to partially damp out this signature, such that the warming is largely offset by vertical diffusion (Fig. 16g). As explained in previous studies (Reintges et al. 2017; Hogg et al. 2017; Cheon et al. 2018; Campbell et al. 2019), the deep ocean convection that occurs over the Ross Sea in the 0.1° case may be linked to a local open polynya triggered by a significant sea ice decrease, which accelerates the oceanic heat loss to the atmosphere.

Furthermore, there are some additional prominent changes in the Southern Ocean across different model resolutions. With the Southern Hemisphere westerly winds increased in magnitude by 15%, the time scale of mesoscale eddy response is ~5 years in the 0.1° case. The MLD anomalies at midlatitudes show opposing responses to the wind strengthening and heating: MLD first deepens due to enhanced vertical mixing and northward Ekman transport during years 1–2, and then shoals due to enhanced surface stratification during years 5–10. Both of these MLD responses are more sensitive to the perturbed forcing in the 1° case than in the 0.1° case. Some deep MLD anomalies develop around Antarctica in the 0.1° case, which corresponds to the significantly increased warm temperature advection driven by anomalous Ekman upwelling. The SST changes around Antarctica largely control the simulated variations in sea ice. Consistent with the development of extensive SST warming, due to resolved vertical temperature gradients at high latitudes, the sea ice decreases more rapidly in the higher-resolution model.

Although idealized wind and thermal forcing can provide an explanation for some observed changes across the Southern Ocean, other issues could also be further considered. For example, our wind and thermal forcing perturbations are relatively strong, more typical of the expected upcoming few decades of change than the recent combined effect of ozone depletion and increasing greenhouse gases. This idealized rate of warming and wind change gives rise to a rapid transition from a cooling phase to a warming phase, particularly in the south Indian Ocean. Recent studies have investigated the importance of broad-scale surface freshening around Antarctica (Purich et al. 2018; Moorman et al. 2020; Rye et al. 2020), which has been attributed to both sea ice transport (Haumann et al. 2016), as well as ice-sheet and ice-shelf melt and iceberg fluxes (Bintanja et al. 2013; Swart and Fyfe 2013; Pauling et al. 2016). Moreover, changes in salinity dominated by future increases in precipitation under global warming may coherently vary with ocean temperatures in the subduction regions (Bindoff and Mcdougall 1994; Purich et al. 2018; Shi et al. 2020). Our results are consistent with previous studies that find that the air–sea feedbacks (not shown), which can be attributed here to the difference between the linearly increasing near-surface air temperature and the changing SST, act to overall damp SST changes (Armour et al. 2016; Liu et al. 2018). In addition, although we configured the intensified westerly wind forcing to mimic ozone-hole forcing for the models at both coarse and high resolutions, our model comparison results could be different from that with a scenario under ozone depletion in a coupled climate model. For instance, Bitz and Polvani (2012) applied the same ozone depletion forcing for models at both coarse and high resolutions; however, the resulting wind increase in their high-resolution simulation is weaker than that at the coarse resolution. Hence a comparison with their study is somewhat ambiguous, since our ocean–sea ice model forcing is controlled to be identical across resolutions. Overall, our results highlight the model-resolution dependence in simulating the transient response of the Southern Ocean to altered wind and thermal forcing. These findings have implications for future Southern Ocean climate projections, since most CMIP6 models are run using coarse-resolution ocean simulations.

Acknowledgments. We thank Andrew E. Kiss for providing advice on the Consortium for Ocean–Sea Ice Modeling in Australia (COSIMA) ACCESS-OM2 model. QL is supported by the Australian Research Council (ARC) Centre of Excellence for Climate System Science. MHE is supported by the ARC Centre of Excellence for Climate Extremes and the Centre for Southern Hemisphere Ocean Research (CSHOR), a joint research center between QNLM, CSIRO, UNSW, and UTAS. MHE is also supported by the Earth Science and Climate Change Hub of the Australian Government's National Environmental Science Programme (NESP). The model simulations and analysis were conducted on the National Computational Infrastructure (NCI) facility in Canberra, Australia.

Data availability statement. The data sets analyzed in this study are all publicly available. Model components are all open source. The ACCESS-OM2 and ACCESS-OM2-01 model simulation output will be stored on the COSIMA data collection website at https://doi.org/10.4225/41/5a2dc8543105a. The JRA55-do v1.3 data used to force the model simulation were obtained for the period 1990–91 at https://climate.mri-jma.go.jp/~htsujino/jra55do.html. SOSE data were obtained for the period 2005–10 from the Scripps website at https://climatedataguide.ucar.edu/climate-data/southern-ocean-state-estimate-sose. The Roemmich-Gilson Argo data were obtained for the period 2004–18 at https://sio-argo.ucsd.edu/RG_Climatology.html. The Argo-float-based MLD data were obtained for the period 2000–19 at http://mixedlayer.ucsd.edu.

REFERENCES

Abernathey, R., and D. Ferreira, 2015: Southern Ocean isopycnal mixing and ventilation changes driven by winds. *Geophys. Res. Lett.*, **42**, 10 357–10 365, https://doi.org/10.1002/2015GL066238.

——, J. Marshall, and D. Ferreira, 2011: The dependence of Southern Ocean meridional overturning on wind stress. *J. Phys. Oceanogr.*, **41**, 2261–2278, https://doi.org/10.1175/JPO-D-11-023.1.

Abram, N. J., R. Mulvaney, F. Vimeux, S. J. Phipps, J. Turner, and M. H. England, 2014: Evolution of the Southern Annular Mode during the past millennium. *Nat. Climate Change*, **4**, 564–569, https://doi.org/10.1038/nclimate2235.

Armour, K. C., J. Marshall, J. R. Scott, A. Donohoe, and E. R. Newsom, 2016: Southern Ocean warming delayed by circumpolar upwelling and equatorward transport. *Nat. Geosci.*, **9**, 549–554, https://doi.org/10.1038/ngeo2731.

Banerjee, A., J. C. Fyfe, L. M. Polvani, D. Waugh, and K.-L. Chang, 2020: A pause in Southern Hemisphere circulation trends due to the Montreal Protocol. *Nature*, **579**, 544–548, https://doi.org/10.1038/s41586-020-2120-4.

Bindoff, N. L., and T. J. Mcdougall, 1994: Diagnosing climate change and ocean ventilation using hydrographic data. *J. Phys. Oceanogr.*, **24**, 1137–1152, https://doi.org/10.1175/1520-0485(1994)024<1137:DCCAOV>2.0.CO;2.

Bintanja, R., G. J. van Oldenborgh, S. S. Drijfhout, B. Wouters, and C. A. Katsman, 2013: Important role for ocean warming and increased ice-shelf melt in Antarctic sea-ice expansion. *Nat. Geosci.*, **6**, 376–379, https://doi.org/10.1038/ngeo1767.

Bishop, S. P., P. R. Gent, F. O. Bryan, A. F. Thompson, M. C. Long, and R. Abernathey, 2016: Southern Ocean overturning compensation in an eddy-resolving climate simulation. *J. Phys. Oceanogr.*, **46**, 1575–1592, https://doi.org/10.1175/JPO-D-15-0177.1.

Bitz, C. M., and L. M. Polvani, 2012: Antarctic climate response to stratospheric ozone depletion in a fine resolution ocean climate model. *Geophys. Res. Lett.*, **39**, L20705, https://doi.org/10.1029/2012GL053393.

Cai, W., T. Cowan, S. Godfrey, and S. Wijffels, 2010: Simulations of processes associated with the fast warming rate of the southern midlatitude ocean. *J. Climate*, **23**, 197–206, https://doi.org/10.1175/2009JCLI3081.1.

Campbell, E. C., E. A. Wilson, G. W. K. Moore, S. C. Riser, C. E. Brayton, M. R. Mazloff, and L. D. Talley, 2019: Antarctic offshore polynyas linked to Southern Hemisphere climate anomalies. *Nature*, **570**, 319–325, https://doi.org/10.1038/s41586-019-1294-0.

Cheon, W. G., C.-B. Cho, A. L. Gordon, Y. H. Kim, and Y.-G. Park, 2018: The role of oscillating Southern Hemisphere westerly winds: Southern Ocean coastal and open-ocean polynyas. *J. Climate*, **31**, 1053–1073, https://doi.org/10.1175/JCLI-D-17-0237.1.

de Boyer Montégut, C., G. Madec, A. S. Fischer, A. Lazar, and D. Iudicone, 2004: Mixed layer depth over the global ocean: An examination of profile data and a profile-based climatology. *J. Geophys. Res.*, **109**, C12003, https://doi.org/10.1029/2004JC002378.

Doddridge, E. W., J. Marshall, H. Song, J.-M. Campin, M. Kelley, and L. Nazarenko, 2019: Eddy compensation dampens Southern Ocean sea surface temperature response to westerly wind trends. *Geophys. Res. Lett.*, **46**, 4365–4377, https://doi.org/10.1029/2019GL082758.

Dong, S., J. Sprintall, S. T. Gille, and L. Talley, 2008: Southern Ocean mixed-layer depth from Argo float profiles. *J. Geophys. Res.*, **113**, C06013, https://doi.org/10.1029/2006JC004051.

Döös, K., and D. J. Webb, 1994: The Deacon cell and the other meridional cells of the Southern Ocean. *J. Phys. Oceanogr.*, **24**, 429–442, https://doi.org/10.1175/1520-0485(1994)024<0429:TDCATO>2.0.CO;2.

Downes, S. M., A. S. Budnick, J. L. Sarmiento, and R. Farneti, 2011: Impacts of wind stress on the Antarctic Circumpolar Current fronts and associated subduction. *Geophys. Res. Lett.*, **38**, L11605, https://doi.org/10.1029/2011GL047668.

Durack, P. J., S. E. Wijffels, and R. J. Matear, 2012: Ocean salinities reveal strong global water cycle intensification during 1950 to 2000. *Science*, **336**, 455–458, https://doi.org/10.1126/science.1212222.

England, M. H., J. S. Godfrey, A. C. Hirst, and M. Tomczak, 1993: The mechanism for Antarctic Intermediate Water renewal in a world ocean model. *J. Phys. Oceanogr.*, **23**, 1553–1560, https://doi.org/10.1175/1520-0485(1993)023<1553:TMFAIW>2.0.CO;2.

Ferreira, D., J. Marshall, C. M. Bitz, S. Solomon, and A. Plumb, 2015: Antarctic ocean and sea ice response to ozone depletion: A two-time-scale problem. *J. Climate*, **28**, 1206–1226, https://doi.org/10.1175/JCLI-D-14-00313.1.

Fraedrich, K., U. Luksch, and R. Blender, 2004: 1/*f* model for long-time memory of the ocean surface temperature. *Phys. Rev. E*, **70**, 037301, https://doi.org/10.1103/PhysRevE.70.037301.

Frölicher, T. L., J. L. Sarmiento, D. J. Paynter, J. P. Dunne, J. P. Krasting, and M. Winton, 2015: Dominance of the Southern Ocean in anthropogenic carbon and heat uptake in CMIP5 models. *J. Climate*, **28**, 862–886, https://doi.org/10.1175/JCLI-D-14-00117.1.

Gent, P. R., 2011: The Gent–McWilliams parameterization: 20/20 hindsight. *Ocean Modell.*, **39**, 2–9, https://doi.org/10.1016/j.ocemod.2010.08.002.

——, and J. C. McWilliams, 1990: Isopycnal mixing in ocean circulation models. *J. Phys. Oceanogr.*, **20**, 150–155, https://doi.org/10.1175/1520-0485(1990)020<0150:IMIOCM>2.0.CO;2.

——, J. Willebrand, T. J. McDougall, and J. C. McWilliams, 1995: Parameterizing eddy-induced tracer transports in ocean circulation models. *J. Phys. Oceanogr.*, **25**, 463–474, https://doi.org/10.1175/1520-0485(1995)025<0463:PEITTI>2.0.CO;2.

Gille, S. T., 2002: Warming of the Southern Ocean since the 1950s. *Science*, **295**, 1275–1277, https://doi.org/10.1126/science.1065863.

Gillett, N. P., and D. W. J. Thompson, 2003: Simulation of recent Southern Hemisphere climate change. *Science*, **302**, 273–275, https://doi.org/10.1126/science.1087440.

Gong, D., and S. Wang, 1999: Definition of Antarctic Oscillation index. *Geophys. Res. Lett.*, **26**, 459–462, https://doi.org/10.1029/1999GL900003.

Griffies, S. M., 2012: Elements of the Modular Ocean Model (MOM): 2012 release. Tech. Rep., NOAA/Geophysical Fluid Dynamics Laboratory, xx pp.

——, and Coauthors, 2015: Impacts on ocean heat from transient mesoscale eddies in a hierarchy of climate models. *J. Climate*, **28**, 952–977, https://doi.org/10.1175/JCLI-D-14-00353.1.

Gruber, N., and Coauthors, 2019: The oceanic sink for anthropogenic CO_2 from 1994 to 2007. *Science*, **363**, 1193–1199, https://doi.org/10.1126/science.aau5153.

Hanawa, K., and L. D. Talley, 2001: Mode waters. *Ocean Circulation and Climate: Observing and Modelling the Global Ocean*, 1st ed., G. Siedler, J. Church, and J. Gould, Eds., Academic Press, 373–386.

Haumann, F. A., N. Gruber, M. Münnich, I. Frenger, and S. Kern, 2016: Sea-ice transport driving Southern Ocean salinity and its recent trends. *Nature*, **537**, 89–92, https://doi.org/10.1038/nature19101.

——, ——, and ——, 2020: Sea-ice induced Southern Ocean subsurface warming and surface cooling in a warming climate. *AGU Adv.*, **1**, e2019AV000132, https://doi.org/10.1029/2019AV000132.

Hogg, A. McC., P. Spence, O. A. Saenko, and S. M. Downes, 2017: The energetics of Southern Ocean upwelling. *J. Phys. Oceanogr.*, **47**, 135–153, https://doi.org/10.1175/JPO-D-16-0176.1.

Holte, J., L. D. Talley, J. Gilson, and D. Roemmich, 2017: An Argo mixed layer climatology and database. *Geophys. Res. Lett.*, **44**, 5618–5626, https://doi.org/10.1002/2017GL073426.

Huber, M., R. Tailleux, D. Ferreira, T. Kuhlbrodt, and J. Gregory, 2015: A traceable physical calibration of the vertical advection-

diffusion equation for modeling ocean heat uptake. *Geophys. Res. Lett.*, **42**, 2333–2341, https://doi.org/10.1002/2015GL063383.

Hunke, E. C., W. H. Lipscomb, A. K. Turner, N. Jeffery, and S. Elliott, 2015: CICE: The Los Alamos sea ice model documentation and software user's manual version 5.1. Los Alamos National Laboratory Tech Rep.

Jayne, S. R., and J. Marotzke, 2002: The oceanic eddy heat transport. *J. Phys. Oceanogr.*, **32**, 3328–3345, https://doi.org/10.1175/1520-0485(2002)032<3328:TOEHT>2.0.CO;2.

Jones, J. M., and Coauthors, 2016: Assessing recent trends in high-latitude Southern Hemisphere surface climate. *Nat. Climate Change*, **6**, 917–926, https://doi.org/10.1038/nclimate3103.

Khatiwala, S., F. Primeau, and T. Hall, 2009: Reconstruction of the history of anthropogenic CO_2 concentrations in the ocean. *Nature*, **462**, 346–349, https://doi.org/10.1038/nature08526.

Kirkman, C. H., and C. M. Bitz, 2011: The effect of the sea ice freshwater flux on Southern Ocean temperatures in CCSM3: Deep-ocean warming and delayed surface warming. *J. Climate*, **24**, 2224–2237, https://doi.org/10.1175/2010JCLI3625.1.

Kiss, A. E., and Coauthors, 2020: ACCESS-OM2 v1.0: A global ocean–sea ice model at three resolutions. *Geosci. Model Dev.*, **13**, 401–442, https://doi.org/10.5194/gmd-13-401-2020.

Kostov, Y., J. Marshall, U. Hausmann, K. C. Armour, D. Ferreira, and M. M. Holland, 2017: Fast and slow responses of Southern Ocean sea surface temperature to SAM in coupled climate models. *Climate Dyn.*, **48**, 1595–1609, https://doi.org/10.1007/s00382-016-3162-z.

——, D. Ferreira, K. C. Armour, and J. Marshall, 2018: Contributions of greenhouse gas forcing and the southern annular mode to historical Southern Ocean surface temperature trends. *Geophys. Res. Lett.*, **45**, 1086–1097, https://doi.org/10.1002/2017GL074964.

Large, W. G., J. C. McWilliams, and S. C. Doney, 1994: Oceanic vertical mixing: A review and a model with a nonlocal boundary layer parameterization. *Rev. Geophys.*, **32**, 363–403, https://doi.org/10.1029/94RG01872.

Levitus, S., and Coauthors, 2012: World Ocean heat content and thermosteric sea level change (0–2000 m), 1955–2010. *Geophys. Res. Lett.*, **39**, L10603, https://doi.org/10.1029/2012GL051106..

Li, Q., and S. Lee, 2017: A mechanism of mixed layer formation in the Indo–western Pacific Southern Ocean: Preconditioning by an eddy-driven jet-scale overturning circulation. *J. Phys. Oceanogr.*, **47**, 2755–2772, https://doi.org/10.1175/JPO-D-17-0006.1.

——, ——, and M. Mazloff, 2018: Evidence of jet-scale overturning ocean circulations in Argo float trajectories. *Geophys. Res. Lett.*, **45**, 11 866–11 874, https://doi.org/10.1029/2018GL078950.

Limpasuvan, V., and D. L. Hartmann, 1999: Eddies and the annular modes of climate variability. *Geophys. Res. Lett.*, **26**, 3133–3136, https://doi.org/10.1029/1999GL010478.

Liu, W., J. Lu, S.-P. Xie, and A. Fedorov, 2018: Southern Ocean heat uptake, redistribution, and storage in a warming climate: The role of meridional overturning circulation. *J. Climate*, **31**, 4727–4743, https://doi.org/10.1175/JCLI-D-17-0761.1.

Lumpkin, R., and K. Speer, 2007: Global ocean meridional overturning. *J. Phys. Oceanogr.*, **37**, 2550–2562, https://doi.org/10.1175/JPO3130.1.

Marshall, G. J., P. A. Stott, J. Turner, W. M. Connolley, J. C. King, and T. A. Lachlan-Cope, 2004: Causes of exceptional atmospheric circulation changes in the Southern Hemisphere. *Geophys. Res. Lett.*, **31**, L14205, https://doi.org/10.1029/2004GL019952.

Marshall, J., and T. Radko, 2003: Residual-mean solutions for the Antarctic Circumpolar Current and its associated overturning circulation. *J. Phys. Oceanogr.*, **33**, 2341–2354, https://doi.org/10.1175/1520-0485(2003)033<2341:RSFTAC>2.0.CO;2.

——, and K. Speer, 2012: Closure of the meridional overturning circulation through Southern Ocean upwelling. *Nat. Geosci.*, **5**, 171–180, https://doi.org/10.1038/ngeo1391.

——, K. C. Armour, J. R. Scott, Y. Kostov, U. Hausmann, D. Ferreira, T. G. Shepherd, and C. M. Bitz, 2014: The ocean's role in polar climate change: Asymmetric Arctic and Antarctic responses to greenhouse gas and ozone forcing. *Philos. Trans. Roy. Soc.*, **372A**, 20130040, https://doi.org/10.1098/rsta.2013.0040.

Mazloff, M. R., P. Heimbach, and C. Wunsch, 2010: An eddy-permitting Southern Ocean state estimate. *J. Phys. Oceanogr.*, **40**, 880–899, https://doi.org/10.1175/2009JPO4236.1.

McCartney, M. S., 1977: Subantarctic Mode Water. *A Voyage of Discovery: George Deacon 70th Anniversary Volume*, M. V. Angel, Ed, Pergamon Press, 103–119.

McDougall, T. J., and P. M. Barker, 2011: Getting started with TEOS-10 and the Gibbs Seawater (GSW) Oceanographic Toolbox. SCOR/IAPSO WG127, 28 pp.

Meredith, M. P., and A. M. Hogg, 2006: Circumpolar response of Southern Ocean eddy activity to a change in the southern annular mode. *Geophys. Res. Lett.*, **33**, L16608, https://doi.org/10.1029/2006GL026499.

Moorman, R., A. K. Morrison, and A. McC. Hogg, 2020: Thermal responses to Antarctic ice shelf melt in an eddy-rich global ocean–sea ice model. *J. Climate*, **33**, 6599–6620, https://doi.org/10.1175/JCLI-D-19-0846.1.

Morrison, A. K., T. L. Frölicher, and J. L. Sarmiento, 2015: Upwelling in the Southern Ocean. *Phys. Today*, **68**, 27–32, https://doi.org/10.1063/PT.3.2654.

Nowlin, W. D., Jr., and J. M. Klinck, 1986: The physics of the Antarctic Circumpolar Current. *Rev. Geophys.*, **24**, 469–491, https://doi.org/10.1029/RG024i003p00469.

Orsi, A. H., T. Whitworth, and W. D. Nowlin, 1995: On the meridional extent and fronts of the Antarctic Circumpolar Current. *Deep-Sea Res. I*, **42**, 641–673, https://doi.org/10.1016/0967-0637(95)00021-W.

Panassa, E., C. Völker, D. Wolf-Gladrow, and J. Hauck, 2018: Drivers of interannual variability of summer mixed layer depth in the Southern Ocean between 2002 and 2011. *J. Geophys. Res. Oceans*, **123**, 5077–5090, https://doi.org/10.1029/2018JC013901.

Pauling, A. G., C. M. Bitz, I. J. Smith, and P. J. Langhorne, 2016: The response of the Southern Ocean and Antarctic sea ice to freshwater from ice shelves in an Earth system model. *J. Climate*, **29**, 1655–1672, https://doi.org/10.1175/JCLI-D-15-0501.1.

Polvani, L. M., D. W. Waugh, G. J. P. Correa, and S.-W. Son, 2011: Stratospheric ozone depletion: The main driver of twentieth-century atmospheric circulation changes in the Southern Hemisphere. *J. Climate*, **24**, 795–812, https://doi.org/10.1175/2010JCLI3772.1.

Primeau, F. W., and M. Holzer, 2006: The ocean's memory of the atmosphere: Residence-time and ventilation-rate distributions of water masses. *J. Phys. Oceanogr.*, **36**, 1439–1456, https://doi.org/10.1175/JPO2919.1.

Purich, A., W. Cai, M. H. England, and T. Cowan, 2016: Evidence for link between modelled trends in Antarctic sea ice and underestimated westerly wind changes. *Nat. Commun.*, **7**, 10409, https://doi.org/10.1038/ncomms10409.

——, M. H. England, W. Cai, A. Sullivan, and P. J. Durack, 2018: Impacts of broad-scale surface freshening of the Southern Ocean in a coupled climate model. *J. Climate*, **31**, 2613–2632, https://doi.org/10.1175/JCLI-D-17-0092.1.

Purkey, S. G., and G. C. Johnson, 2013: Antarctic Bottom Water warming and freshening: Contributions to sea level rise, ocean

freshwater budgets, and global heat gain. *J. Climate*, **26**, 6105–6122, https://doi.org/10.1175/JCLI-D-12-00834.1.

Qu, X., and A. Hall, 2005: Surface contribution to planetary albedo variability in cryosphere regions. *J. Climate*, **18**, 5239–5252, https://doi.org/10.1175/JCLI3555.1.

Redi, M. H., 1982: Oceanic isopycnal mixing by coordinate rotation. *J. Phys. Oceanogr.*, **12**, 1154–1158, https://doi.org/10.1175/1520-0485(1982)012<1154:OIMBCR>2.0.CO;2.

Reintges, A., T. Martin, M. Latif, and W. Park, 2017: Physical controls of Southern Ocean deep-convection variability in CMIP5 models and the Kiel Climate Model. *Geophys. Res. Lett.*, **44**, 6951–6958, https://doi.org/10.1002/2017GL074087.

Rintoul, S. R., and M. H. England, 2002: Ekman transport dominates local air–sea fluxes in driving variability of Subantarctic Mode Water. *J. Phys. Oceanogr.*, **32**, 1308–1321, https://doi.org/10.1175/1520-0485(2002)032<1308:ETDLAS>2.0.CO;2.

Roemmich, D., and J. Gilson, 2009: The 2004–2008 mean and annual cycle of temperature, salinity, and steric height in the global ocean from the Argo program. *Prog. Oceanogr.*, **82**, 81–100, https://doi.org/10.1016/j.pocean.2009.03.004.

——, J. Church, J. Gilson, D. Monselesan, P. Sutton, and S. Wijffels, 2015: Unabated planetary warming and its ocean structure since 2006. *Nat. Climate Change*, **5**, 240–245, https://doi.org/10.1038/nclimate2513.

Rye, C. D., J. Marshall, M. Kelley, G. Russell, L. S. Nazarenko, Y. Kostov, G. A. Schmidt, and J. Hansen, 2020: Antarctic glacial melt as a driver of recent Southern Ocean climate trends. *Geophys. Res. Lett.*, **47**, e2019GL086892, https://doi.org/10.1029/2019GL086892..

Sallée, J.-B., R. J. Matear, S. R. Rintoul, and A. Lenton, 2012: Localized subduction of anthropogenic carbon dioxide in the Southern Hemisphere oceans. *Nat. Geosci.*, **5**, 579–584, https://doi.org/10.1038/ngeo1523.

Sarmiento, J. L., N. Gruber, M. A. Brzezinski, and J. P. Dunne, 2004: High-latitude controls of thermocline nutrients and low-latitude biological productivity. *Nature*, **427**, 56–60, https://doi.org/10.1038/nature02127.

Shi, J.-R., L. D. Talley, S.-P. Xie, W. Liu, and S. T. Gille, 2020: Effects of buoyancy and wind forcing on Southern Ocean climate change. *J. Climate*, **33**, 10 003–10 020, https://doi.org/10.1175/JCLI-D-19-0877.1.

Sloyan, B. M., and S. R. Rintoul, 2001: Circulation, renewal, and modification of Antarctic Mode and Intermediate Water. *J. Phys. Oceanogr.*, **31**, 1005–1030, https://doi.org/10.1175/1520-0485(2001)031<1005:CRAMOA>2.0.CO;2.

Snow, K., A. M. Hogg, B. M. Sloyan, and S. M. Downes, 2015: Sensitivity of Antarctic Bottom Water to changes in surface buoyancy fluxes. *J. Climate*, **29**, 313–330, https://doi.org/10.1175/JCLI-D-15-0467.1.

Solomon, S., D. J. Ivy, D. Kinnison, M. J. Mills, R. R. Neely, and A. Schmidt, 2016: Emergence of healing in the Antarctic ozone layer. *Science*, **353**, 269–274, https://doi.org/10.1126/science.aae0061.

Stewart, K. D., and A. M. Hogg, 2019: Southern Ocean heat and momentum uptake are sensitive to the vertical resolution at the ocean surface. *Ocean Modell.*, **143**, 101456, https://doi.org/10.1016/j.ocemod.2019.101456.

——, and Coauthors, 2020: JRA55-do-based repeat year forcing datasets for driving ocean–sea-ice models. *Ocean Modell.*, **147**, 101557, https://doi.org/10.1016/j.ocemod.2019.101557.

Swart, N. C., and J. C. Fyfe, 2013: The influence of recent Antarctic ice sheet retreat on simulated sea ice area trends. *Geophys. Res. Lett.*, **40**, 4328–4332, https://doi.org/10.1002/grl.50820.

——, S. T. Gille, J. C. Fyfe, and N. P. Gillett, 2018: Recent Southern Ocean warming and freshening driven by greenhouse gas emissions and ozone depletion. *Nat. Geosci.*, **11**, 836–841, https://doi.org/10.1038/s41561-018-0226-1.

Talley, L., and Coauthors, 2016: Changes in ocean heat, carbon content, and ventilation: A review of the first decade of GO-SHIP global repeat hydrography. *Annu. Rev. Mar. Sci.*, **8**, 185–215, https://doi.org/10.1146/annurev-marine-052915-100829.

Thompson, D. W. J., and J. M. Wallace, 2000: Annular modes in the extratropical circulation. Part I: Month-to-month variability. *J. Climate*, **13**, 1000–1016, https://doi.org/10.1175/1520-0442(2000)013<1000:AMITEC>2.0.CO;2.

——, S. Solomon, P. J. Kushner, M. H. England, K. M. Grise, and D. J. Karoly, 2011: Signatures of the Antarctic ozone hole in Southern Hemisphere surface climate change. *Nat. Geosci.*, **4**, 741–749, https://doi.org/10.1038/ngeo1296.

Toggweiler, J. R., and J. Russell, 2008: Ocean circulation in a warming climate. *Nature*, **451**, 286–288, https://doi.org/10.1038/nature06590.

Treguier, A. M., J. Le Sommer, J. M. Molines, and B. de Cuevas, 2010: Response of the Southern Ocean to the southern annular mode: Interannual variability and multidecadal trend. *J. Phys. Oceanogr.*, **40**, 1659–1668, https://doi.org/10.1175/2010JPO4364.1.

Tsujino, H., and Coauthors, 2018: JRA-55 based surface dataset for driving ocean–sea-ice models (JRA55-do). *Ocean Modell.*, **130**, 79–139, https://doi.org/10.1016/j.ocemod.2018.07.002.

Waugh, D. W., C. I. Garfinkel, and L. M. Polvani, 2015: Drivers of the recent tropical expansion in the Southern Hemisphere: Changing SSTs or ozone depletion? *J. Climate*, **28**, 6581–6586, https://doi.org/10.1175/JCLI-D-15-0138.1.

——, A. McC. Hogg, P. Spence, M. H. England, and T. W. N. Haine, 2019: Response of Southern Ocean ventilation to changes in midlatitude westerly winds. *J. Climate*, **32**, 5345–5361, https://doi.org/10.1175/JCLI-D-19-0039.1.

Young, I. R., and A. Ribal, 2019: Multiplatform evaluation of global trends in wind speed and wave height. *Science*, **364**, 548–552, https://doi.org/10.1126/science.aav9527.